

RESEARCH ARTICLE | AUGUST 04 2025

## Edge formation in intermittent slot-die coating for lithium-ion battery electrode

Xiaosong Gong (弓晓松); Bin Li (李斌); Jiaye Yao (姚佳烨); Fei Yan (闫飞) ; Xiaozhong Du (杜晓钟)  



*Physics of Fluids* 37, 082103 (2025)  
<https://doi.org/10.1063/5.0279043>



### Articles You May Be Interested In

Dynamical wetting transition of a stretched liquid bridge

*Physics of Fluids* (March 2024)

Data-driven modeling of apparent added mass force in filtered two-fluid models for densely loaded gas-particle flows

*Physics of Fluids* (April 2025)

Study of burst mode for enhancing the ps-laser cutting performance of lithium-ion battery electrodes

*J. Laser Appl.* (September 2024)



**Physics of Fluids**  
Special Topics  
Open for Submissions

[Learn More](#)

 AIP Publishing

# Edge formation in intermittent slot-die coating for lithium-ion battery electrode

Cite as: Phys. Fluids 37, 082103 (2025); doi: 10.1063/5.0279043

Submitted: 5 May 2025 · Accepted: 26 June 2025 ·

Published Online: 4 August 2025



View Online



Export Citation



CrossMark

Xiaosong Gong (弓晓松),<sup>1</sup> Bin Li (李斌),<sup>1</sup> Jiaye Yao (姚佳烨),<sup>1</sup> Fei Yan (闫飞),<sup>2</sup> and Xiaozhong Du (杜晓钟),<sup>1,3,a)</sup>

## AFFILIATIONS

<sup>1</sup>School of Mechanical Engineering, Taiyuan University of Science and Technology, Taiyuan 030024, China

<sup>2</sup>College of Automobile Engineering, Wuhan University of Technology, Wuhan 430070, China

<sup>3</sup>School of Energy and Materials Engineering, Taiyuan University of Science and Technology, Taiyuan 030024, China

<sup>a)</sup>Author to whom correspondence should be addressed: [xiaozhong\\_d@163.com](mailto:xiaozhong_d@163.com)

## ABSTRACT

In the intermittent slot-die coating process for lithium-ion batteries, precise control of the electrode edges during the rapid start–stop phase presents a significant challenge. This study reveals the formation mechanisms of the leading and trailing edges during the coating process by integrating numerical simulations with experimental methods. Four machine learning models are developed to predict the edge dimensions based on high-fidelity simulation datasets. The results indicate that the morphology and evolution stages of the trailing edge are controlled by the stretching, movement, and fracture processes of the upstream meniscus, resulting in three distinct length regimes governed by the capillary number ( $Ca$ ). The leading-edge height is influenced by the flow structure within the coating gap and the position of the downstream wetting line, resulting in four distinct height regimes. When viscous forces dominate, the accumulation of residual slurry increases the leading-edge height. However, under high-speed coating conditions, residual slurry tends to reduce it. Additionally, four rupture mechanisms of the meniscus liquid bridge were identified, leading to the formation of fingerlike edges and stripe patterns at the trailing edge. Leading-edge burrs and tilting resulted from evolving residual slurry during re-initiation. Extreme Gradient Boosting demonstrated the highest predictive accuracy, achieving  $R^2$  values of 0.983, 0.958, and 0.9135 for leading-edge height difference, trailing-edge length, and evolution stage, respectively. SHapley Additive exPlanations analysis identified  $Ca$  and coating speed as the dominant factors in edge quality. These findings offer key insights for optimizing high-precision patterned coating processes.

Published under an exclusive license by AIP Publishing. <https://doi.org/10.1063/5.0279043>

## I. INTRODUCTION

Intermittent slot-die coating is a high-precision patterning technique widely applied in advanced manufacturing domains such as lithium-ion battery electrodes,<sup>1</sup> flexible electronics,<sup>2</sup> organic light emitting diode (OLED) displays,<sup>3</sup> and perovskite solar cells.<sup>4</sup> These applications impose stringent demands on the precise control of edge morphology during the coating process. For instance, in OLED display fabrication, edge accuracy directly influences pattern resolution and overall device integration. In perovskite photovoltaic devices, precise stacking and alignment of multilayer structures are essential to prevent interlayer contamination and to ensure high-efficiency, stable optoelectronic performance. Moreover, by enabling fine control over liquid bridge dynamics during rapid start–stop transitions, intermittent slot-die coating offers unique advantages and strong potential for the scalable fabrication of micro-structured sensors<sup>5</sup> and periodic functional coatings.<sup>6</sup> For lithium-ion battery (LIB) electrodes, due to the requirements of battery stacking and tab welding processes, sequential start–stop

control of the inlet flow rate in the slot die is necessary.<sup>7,8</sup> In a typical intermittent coating process (as shown in Fig. 1), the slurry is pumped into the coating gap between the backing roller and the die lip, forming a stable coating bead region surrounded by upstream and downstream menisci. A uniform thin film is then formed starting from the downstream meniscus. However, during the startup and stop moments of coating, dynamic pressure variations and fluctuations in slurry viscosity often trigger defects at the leading and trailing edges. These defects not only cause uneven pressure distribution in subsequent calendering processes but also directly impact the stacking accuracy of the electrode sheets, thus significantly affecting the consistency of the battery.<sup>9</sup>

During the coating process, dynamic flow near the die exit and downstream is of particular concern. The coating bead region is primarily controlled by three forces: capillary forces caused by surface tension, viscous forces due to substrate movement, and inertial forces resulting from high-speed feeding. The balance between these forces is crucial for the rupture and reformation of the coating bead region.

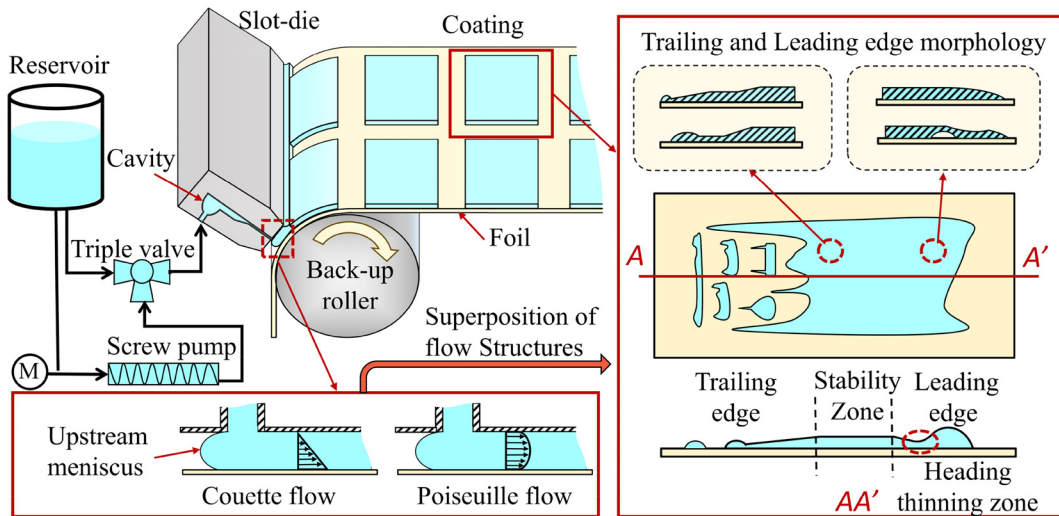


FIG. 1. Process sketch of slot-die coating.

Several analytical models have been proposed to determine the stable coating conditions, including capillary models,<sup>10</sup> viscous models,<sup>11</sup> capillary-viscous models,<sup>12</sup> and inertial capillary models.<sup>13</sup> These models generally suggest that the upstream meniscus, near the slot-die exit, is the primary factor contributing to instability in the coating bead region. Previous studies have shown that enhancing the rigidity and viscosity of the upstream meniscus helps improve the stability of the coating bead region.<sup>14,15</sup> Fang *et al.*<sup>16</sup> found that vortices at the bottom of the upstream meniscus cause dynamic contact angle fluctuations between the slurry and substrate, leading to air entrainment in the upstream meniscus. This indicates that the motion characteristics of the upstream meniscus play a critical role in the stability of the coating bead region.

The formation process of the trailing edge is closely related to the drainage process of the slurry in the coating bead region, resembling the gradual liquid transfer between two parallel plates.<sup>17–20</sup> Tan *et al.*<sup>21</sup> found that the tail length of a Newtonian fluid in coating is closely related to the capillary number ( $Ca$ , viscous force/surface tension). Maza and Carvalho<sup>22</sup> pointed out that limiting the movement of the wetting line of the downstream meniscus can promote faster rupture of the coating bead, thereby reducing the tail length. Diehm *et al.*<sup>9</sup> studied the effect of anode slurry at coating speeds up to 50 m/min and a wet film thickness of 400  $\mu\text{m}$  on the quality of the coating's leading and trailing edges. Notably, they found that regardless of the coating speed, the length of the leading and trailing edges remained constant, attributing this to the complete drainage of the slurry. Schmitt *et al.*<sup>23</sup> demonstrated that the wet film thickness of the coating is directly influenced by the die pressure distribution. To ensure well-defined leading and trailing edges, it is essential to minimize the ramp-up and ramp-down durations of the die pressure. Chang *et al.*<sup>24</sup> showed that any factor that increases the volume of the coating bead will prolong the startup time. Pan *et al.*<sup>25</sup> reached similar conclusions and identified four patterns of meniscus formation for the upstream and downstream menisci. Although the impact of these meniscus formation patterns on the height of the leading edge remains unclear, it can be anticipated

that when inertial forces dominate, the downstream meniscus will form first. When the slurry exits at high speeds, the die geometry cannot restrict the movement of the wetting line. At this point, the size of the coating gap will have a significant effect. Park *et al.*<sup>26</sup> in a dual-layer coating process, effectively reduced coating edge defects by controlling the start-stop timing between the top and bottom layer inlet flows. In industry, methods such as slurry backflow, gap adjustment, or a combination of both can also achieve sharp stop edges.<sup>27</sup> However, these methods are typically only applicable at lower coating speeds. Therefore, the quantitative relationship between the rupture and reformation process of the coating bead region and edge features still requires further investigation.

During the start-stop process of intermittent coating, the self-organized patterns that appear are often considered undesirable defects. The formation mechanism is similar to the meniscus instability under low flow conditions. Under low flow conditions, the upstream meniscus retreats excessively to maintain the pressure drop on the coating bead, resulting in three-dimensional and unstable flow. During this process, the meniscus often ruptures, leading to the formation of alternating coated and uncoated stripes on the substrate. This defect is typically referred to as "stream" or "rib." Experiments by Kasischke *et al.*<sup>28</sup> found that the transition of the stripe pattern is highly dependent on the coating speed and viscosity. At high viscosity, the stripes are perpendicular to the coating direction, while at low viscosity, they are arranged in parallel. Additionally, an increase in the coating gap height leads to the appearance of parallel stripes, with the stripe period decreasing as the gap height increases. Tewes *et al.*<sup>29</sup> observed similar pattern phenomena in dip-coating studies and believed these were closely related to the instability of the meniscus and spinodal dewetting.<sup>30–32</sup> Raupp *et al.*<sup>33</sup> pointed out that increasing viscosity and decreasing surface tension can suppress the self-organized merging of stripes in the width direction. Parsekian and Harris<sup>34</sup> found that the formation of conical patterns at the leading and trailing edges is closely related to changes in residual slurry volume. Bhamidipati *et al.*<sup>35</sup> discovered that in slot-die coating of

shear-thinning fluids, bubble rupture patterns are associated with the morphology of the upstream meniscus, and bubbles entrapped in the meniscus lead to periodic stripes and regularly arranged spots after rupture downstream. Khandavalli and Rothstein<sup>36</sup> showed experimentally that the instability of cross-waves increases with the degree of shear thickening. Schmitt *et al.*<sup>37</sup> observed horizontal and vertical stripe patterns during the coating of anode slurries, suggesting that vertical stripes might result from the shear action within the gap, leading to large particle aggregation and rupture of the downstream meniscus. Periodic horizontal stripes, on the other hand, are associated with periodic disturbances of the coating equipment. Huang *et al.*<sup>38</sup> found that vertical stripes were related to the shrinkage of the downstream meniscus, while spot-like and irregular patterns were linked to the unstable development of the sawtooth dynamic contact line. While previous studies have explored the formation of coating patterns under low-flow conditions, the pattern characteristics resulting from the forced rupture and reformation of the coating bead region have not been fully investigated.

In the simulation of the coating process, computational cost presents a significant challenge for numerical process models, particularly for models with 3D resolution.<sup>39</sup> Physics-based models are often limited by computational complexity, whereas machine learning methods can efficiently extract meaningful features from large, unstructured datasets to uncover relationships among multiple variables.<sup>40,41</sup> As a result, electrode production has recently emerged as a new frontier for machine learning applications.<sup>42</sup> Recent studies have shown<sup>43–46</sup> that data-driven models can replace the laborious parameterization steps in the LIB manufacturing process, requiring only limited underlying physical knowledge. Schnell *et al.*<sup>47</sup> were the first to propose a data mining framework based on real data from battery production lines, investigating the effects of process parameters in five electrode production sub-processes and 11 cell manufacturing sub-processes on the quality of intermediate products, subsequent processes, and final cell quality. Niri *et al.*<sup>48</sup> employed interpretable machine learning methods and systematic statistical analysis to comprehensively assess the complex interdependencies in the slurry coating process. Seo *et al.*<sup>49</sup> optimized mold structures and reduced lateral edge defects in coatings by constructing a computational fluid dynamics (CFD)-based machine learning model. However, due to the challenges in data collection, no predictive model for edge defects in intermittent coating processes has been proposed to date.

Based on these gaps, this study addresses two key research questions: (1) How does the rupture and reformation of the coating bead region influence the formation of leading and trailing edges during intermittent slot-die coating? (2) What types of three-dimensional patterns emerge at the leading and trailing edges during rapid start-stop transitions? To answer these questions, this study integrates numerical simulations with experimental observations to reveal the physical mechanisms governing the stretching, movement, and rupture of the upstream meniscus during the evolution of the trailing edge. It also investigates the relationship between flow structure and the height of the leading edge. Through capillary number analysis, the distribution characteristics of both the trailing-edge length and leading-edge height are systematically identified. The research further elucidates edge effects and the evolution of defects induced by the rupture of the meniscus liquid bridge, with experimental validation confirming the simulation findings. Finally, four machine learning models are developed and trained on high-fidelity simulation datasets to predict edge dimensions based on key process parameters.

## II. EXPERIMENTAL

### A. Numerical simulation

In the intermittent start-stop coating process, the formation of defects is a three-dimensional, transient, incompressible, laminar two-phase flow of gas and liquid. The primary and secondary phases are the air and anode slurry, respectively. The interface between the air and anode slurry is tracked using the volume-of-fluid method.<sup>50</sup> The continuity and momentum equations are summarized as follows:

$$\frac{\partial \alpha_{slurry}}{\partial t} + u_i \frac{\partial \alpha_{slurry}}{\partial x_i} = 0, \quad (1)$$

$$\alpha_{air} = 1 - \alpha_{slurry}, \quad (2)$$

$$\frac{\partial \rho}{\partial t} + \nabla \cdot (\rho \mathbf{u}) = 0, \quad (3)$$

$$\frac{\partial(\rho \mathbf{u})}{\partial t} + \nabla \cdot (\rho \mathbf{u} \mathbf{u}) = -\nabla p + \nabla \cdot [\mu(\nabla \mathbf{u} + \nabla \mathbf{u}^T)] + \rho \mathbf{g} + \mathbf{F}_s, \quad (4)$$

where  $\alpha_{slurry}$  and  $\alpha_{air}$  represent the volume fractions of air and the anode slurry, respectively. The cell is completely filled with air or the anode slurry when  $\alpha_{air} = 1$  or 0, respectively. Where  $\mathbf{u}$  is the velocity tensor,  $\rho$  is the material density.  $\mathbf{p}$  and  $\mathbf{g}$  are the pressure and gravitational force, respectively.

The terms can be calculated as follows:

$$\rho = \alpha_{air} \rho_{air} + \alpha_{slurry} \rho_{slurry}, \quad (5)$$

$$\mu = \alpha_{air} \mu_{air} + \alpha_{slurry} \mu_{slurry}, \quad (6)$$

$$\mathbf{u} = \frac{\alpha_{air} \rho_{air} \mathbf{u}_{air} + \alpha_{slurry} \rho_{slurry} \mathbf{u}_{slurry}}{\rho}, \quad (7)$$

where  $\rho_{air}$  and  $\rho_{slurry}$  are the densities of air and the anode slurry, respectively.  $\mu_{air}$  and  $\mu_{slurry}$  are the viscosities of air and the anode slurry, respectively.  $\mathbf{u}_{air}$  and  $\mathbf{u}_{slurry}$  are the velocity tensors of air and the anode slurry, respectively.

In the momentum equation,  $F_s$  denotes the surface tension source term. This term can be calculated using the continuum surface force (CSF) model proposed by Brackbill *et al.*,<sup>51</sup> as the following Eq. (8) shows:

$$F_s = \sigma \frac{k \nabla \alpha_{slurry} \rho}{0.5(\rho_{air} + \rho_{slurry})}, \quad (8)$$

where  $\sigma$  and  $k$  are the surface tension force and the curvature of the interface, respectively.  $k$  can be computed through the following: The curvature of the interface at any point on the wall boundaries is given by Eq. (9):

$$k = \nabla \cdot \hat{n}, \quad (9)$$

$$\hat{n} = \hat{n}_w \cos \theta_w + \hat{t}_w \sin \theta_w, \quad (10)$$

where  $\hat{n}$  is the unit normal vector to the interface and  $\hat{n}_w$  is normal to the wall.  $\hat{t}_w$  is tangent to the wall.  $\theta_w$  is the contact angle between the slurry and the wall.

### B. Boundary conditions

In this study, we simulated two complete cycles of the intermittent slot-die coating process to capture the dynamic evolution of leading- and trailing-edge patterns at various stages. The boundary

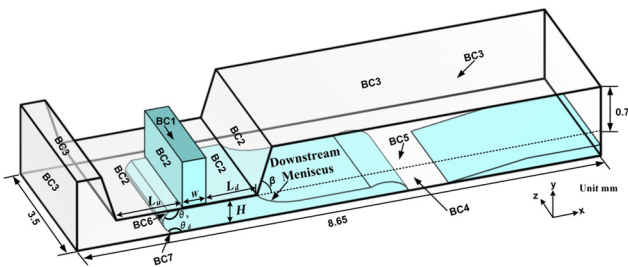


FIG. 2. Boundary conditions of the computational domain.

conditions of the model are illustrated in Fig. 2 and labeled as BC1 to BC7. The die shoulder angle is the complementary angle of  $\beta$  ( $180^\circ - \beta$ ). Similar numerical models incorporating edge effects have also been developed in the previous studies.<sup>52</sup> The material composition and preparation procedure used in this study are consistent with those reported by Huang *et al.*<sup>38</sup> To simplify the computation, the viscosity variation at extremely low shear rates was neglected in the numerical

simulations. The Herschel–Bulkley model ( $\eta_s = \tau_0/\dot{\gamma} + k \cdot \dot{\gamma}^{n-1}$ ) is used to describe the shear rheological behavior of the anode slurry. When the yield stress is zero, the Herschel–Bulkley model reduces to the power-law model ( $\eta_s = k \cdot \dot{\gamma}^{n-1}$ ). During the high-speed coating process, the upstream meniscus at the bottom of the coating bead is subjected to strong shear forces from the moving substrate.<sup>15,16</sup> To prevent abnormal viscosity values, we introduced a very small yield stress coefficient (0.001 Pa) in the model, which has a negligible effect on the rheological properties. Detailed fluid physical parameters are shown in Table I. Given the alternating start and stop actions required by the intermittent coating process, we employed a time-dependent velocity inlet condition (BC1), as described by Eq. (11), where  $x$  denotes the  $x$ -axis coordinate. A steady-state flow field was initially established using a sufficiently developed velocity profile,<sup>38</sup> which then served as the initial condition for the transient simulation. During the start–stop transition process, we applied linear ramp-up or ramp-down velocities to simulate switching, with  $\Delta t$  representing the switching response time. The time  $t_0$  is defined as the moment when the tail completely breaks.

BC1: A time-dependent velocity inlet condition is set at this location

$$V(x) = \begin{cases} \frac{U_{\text{sub}} h_\infty}{W} \left( \frac{2n+1}{n+1} \right) \left( 1 - \left[ \frac{x}{(W/2)} \right]^{\frac{1+n}{n}} \right) & \text{steady} \\ \frac{U_{\text{sub}} h_\infty}{W} \left( \frac{2n+1}{n+1} \right) \left( 1 - \left[ \frac{x}{(W/2)} \right]^{\frac{1+n}{n}} \right) \left( 1 - \frac{t}{\Delta t} \right) & 0 \leq t < \Delta t \\ 0 & \Delta t \leq t < t_0 \\ \frac{U_{\text{sub}} h_\infty}{W} \left( \frac{2n+1}{n+1} \right) \left( 1 - \left[ \frac{x}{(W/2)} \right]^{\frac{1+n}{n}} \right) \left( \frac{t - t_0}{\Delta t} \right) & t_0 \leq t < t_0 + \Delta t \\ \frac{U_{\text{sub}} h_\infty}{W} \left( \frac{2n+1}{n+1} \right) \left( 1 - \left[ \frac{x}{(W/2)} \right]^{\frac{1+n}{n}} \right) & t_0 + \Delta t \leq t. \end{cases} \quad (11)$$

BC2: No-slip and penetration wall boundary conditions are imposed.

BC3: Standard atmospheric pressure outlet.

BC4: A symmetry boundary condition.

BC5: A moving wall condition is applied at this location.

BC6: No-slip and penetration wall boundary conditions are imposed.

BC7: The dynamic contact angle varies based on the dynamic contact line velocity in relation to the capillary number. We use Kistler's approach<sup>53</sup> to determine the fluctuation of the dynamic contact angle

$$\theta_d = f_H \left[ Ca + f_H^{-1}(\theta_{eq}) \right], \quad (12)$$

$$f_H = \cos^{-1} \left\{ 1 - 2 \tanh \left[ 5.16 \left( \frac{x}{1 + 1.31x^{0.99}} \right)^{0.706} \right] \right\}, \quad (13)$$

$$x = Ca + f_H^{-1}(\theta_{eq}), \quad (14)$$

$$Ca = \frac{\mu u_c}{\sigma}, \quad (15)$$

$$u_c = (u_{cell} \cdot n_t) \frac{n_t}{\| n_t \|}, \quad (16)$$

where  $Ca$  is the capillary number. The equilibrium angle is denoted by  $\theta_{eq}$  with a value of  $55.6^\circ$ .  $f_H$  is Hoffman's function.  $u_c$  and  $u_{cell}$  denote the cell velocity in close to the dynamic contact line. We encapsulate Eqs. (12)–(16) into a user-defined function to compute the dynamic contact angle. The meshing method of the model and the validation of its effectiveness are detailed in Appendixes A and B, respectively. In this study, the trailing-edge length is defined as the distance between the first point where the coating thickness reaches 98% of the ideal value and the first point where the coating thickness reaches 2% of the ideal value. The leading-edge height is defined as the maximum coating thickness at the leading edge when it reaches the edge of the computational domain in the  $X$  direction. Table I lists the relevant parameters for the simulation.

**TABLE I.** Details of the parameters used in the simulation.

| Parameters                             | Descriptions                                      | Value              |
|--|---|--------------------|
| Fluid property parameter <sup>38</sup> | Density, $\rho_{slurry}$ (kg/m <sup>3</sup> )     | 1320               |
|  | Surface tension, $\sigma$ (N/m)                   | 0.066              |
|  | Static contact angle (die lip), $\theta_w$ (°)    | 72.5               |
|  | Equilibrium angle (substrate), $\theta_{eq}$ (°)  | 55.6               |
|  | Consistency index, $k$ (Pa s <sup>n</sup> )       | 3.585              |
|  | Shear-thinning index, $n$                         | 0.6322             |
|  | Yield stress $\tau_0$ (Pa)                        | 0.001              |
| Configuration parameter                | Upstream die length, $L_u$ (mm)                   | 1                  |
|  | Downstream die length, $L_d$ (mm)                 | 0.4; 0.7; 1        |
|  | Slot width, $W$ (mm)                              | 0.1; 0.2; 0.3      |
|  | Coating gap, $H$ (mm)                             | 0.2; 0.25; 0.3     |
|  | Complement of the die shoulder angle, $\beta$ (°) | 45; 67.5; 90       |
|  | Response time, $\Delta t$ (s)                     | 0.005; 0.01; 0.015 |
|  | Coating thickness, $h$ ( $\mu$ m)                 | 180; 210; 240      |
| Coating velocity, $U_{sub}$ (m/s)      |   | 0.004–0.8          |

### C. Slot-coating experiments

To investigate the edge effects and pattern evolution of coatings during the intermittent coating process, this study employed a slot-die coating experimental platform as shown in Fig. 3 (Ossila, UK). The platform is equipped with a high-precision injection pump and an

electrically driven movable base, forming a micro-injection system. The base moves horizontally along linear rails via an AC motor, with a speed range of 0.1–50 mm/s. Additionally, the platform facilitates multi-step coating processes, with each intermittent step configured by setting the coating length and slurry flow rate for each sub-step,

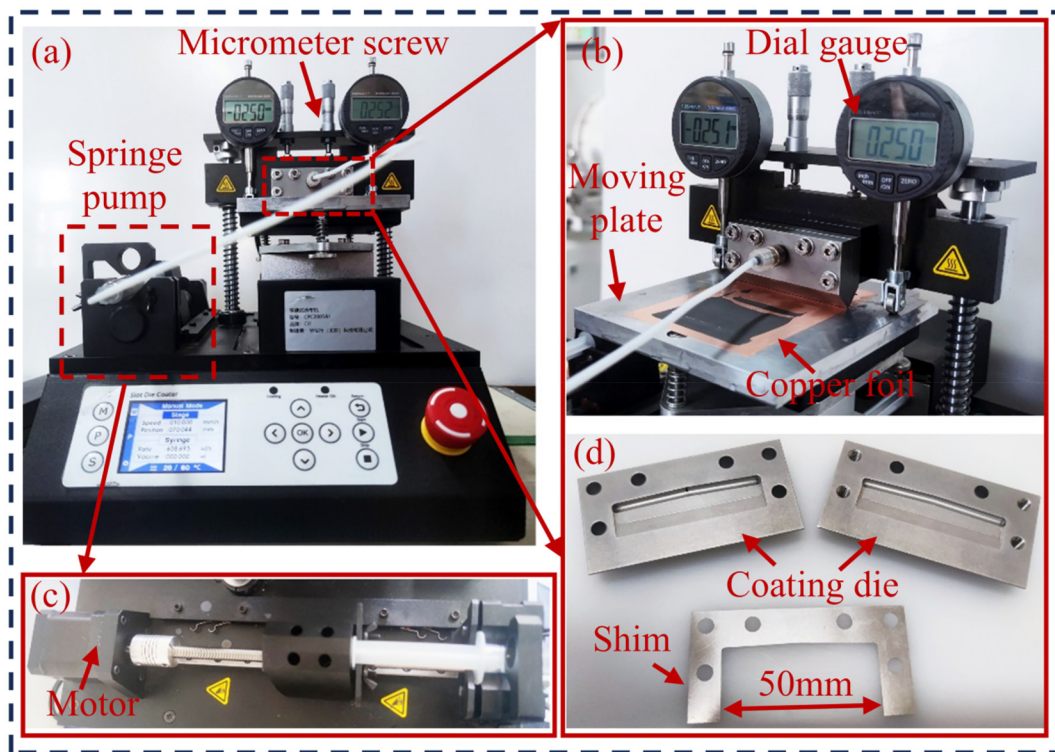


**FIG. 3.** Slot-die coating experiment device: (a) device components, (b) coating process, (c) spring pump, and (d) structure of the coating die.

resulting in coated and uncoated regions. The experimental system employs a hanger-type coating die, comprising an upper and a lower mold. The slot gap ( $W$ ) is set to 0.2 mm using two stainless steel spacers, each 0.1 mm thick. The distance between the die and the substrate is defined as the coating gap ( $H$ ). Two adjustable helical feed structures at the top of the equipment enable precise control of the coating gap, with an accuracy of 0.001 mm. To ensure a stable coating process, according to previous studies,<sup>38</sup> the minimum wet film thickness is approximately 60% of the coating gap. We provided the minimum film thickness for a coating gap of 0.3 mm, as shown in Fig. 14 of Appendix C. It is worth noting that we use the upstream meniscus reaching the slot exit as the critical condition for achieving the minimum film thickness.<sup>12,13</sup> The coating thickness is consistently maintained at 180  $\mu\text{m}$ , with the coating gap adjustable between 0.2 and 0.3 mm. A representative anode material system was chosen for slot-die coating experiments to optimize its industrial applicability. The weight ratios and mixing process of the anode slurry were consistent with previous experiments,<sup>38</sup> ensuring comparability of the experimental conditions.

To identify edge defects under different coating speeds and gaps, the experimental process can be summarized in the following steps:

- (1) Set the base movement speed, coating length, and stop length. To ensure the tail edge develops fully, the length of the uncoated region is set to 40 mm. The coating length for the second cycle is determined based on the distance the base travels in 1 s.
- (2) Adjust the base movement speed and recalculate the anode slurry flow rate to achieve the target coating thickness of 180  $\mu\text{m}$  and repeat step (1).
- (3) Vary the coating gap and repeat steps (1) and (2), recording the edge morphology under different coating speeds.

#### D. Defect prediction based on machine learning prediction models

This section presents machine learning models developed using high-fidelity simulation data, including Extreme Gradient Boosting (XGBoost), multi-layer perceptron (MLP), AdaBoost, and Light

Gradient Boosting Machine (LightGBM). These models were designed to accurately predict the dimensions of leading- and trailing-edge defects, including trailing-edge length, leading-edge height difference, and trailing-edge evolution stage. As illustrated in Fig. 4, the modeling workflow consists of five key steps, encompassing the entire process from high-quality data acquisition to final model evaluation. To enhance model interpretability, the SHAP (SHapley Additive exPlanations) method was employed. K-fold cross-validation is widely recognized as an effective strategy for mitigating overfitting, as it systematically assesses model performance across multiple independent subsets and thereby evaluates generalization to unseen data.<sup>54</sup> In this study, a rigorous fourfold cross-validation strategy was adopted during training to prevent overfitting.

The Extreme Gradient Boosting (XGBoost)<sup>55</sup> algorithm is a highly scalable and computationally efficient machine learning method derived from an optimized gradient boosting framework. It sequentially constructs decision trees, with each subsequent tree specifically designed to minimize the residual errors from preceding trees. Each individual tree in XGBoost functions as a weak learner with limited predictive power; however, when combined into an ensemble, these weak learners produce a robust and powerful predictive model capable of significantly improving prediction accuracy. XGBoost employs regularization terms and utilizes second-order gradients to effectively control model complexity and overfitting, further enhancing its predictive performance. Parallel computation strategies within XGBoost substantially increase computational efficiency. At iteration  $t$ , the predicted output  $\hat{y}_i^{(t)}$  can be defined as follows:

$$\hat{y}_i^{(t)} = \hat{y}_i^{(t-1)} + f_t(x_i), \quad f_t \in \mathcal{F}, \quad (17)$$

where  $\mathcal{F}$  denotes the space of regression trees.  $f_t(x_i)$  denotes the newly constructed tree aimed at reducing the residual errors from iteration. The overall objective function to be minimized is

$$\mathcal{L}^{(t)} = \sum_{i=1}^n [l(y_i, \hat{y}_i^{(t)})] + \sum_{k=1}^t \Omega(f_k), \quad (18)$$

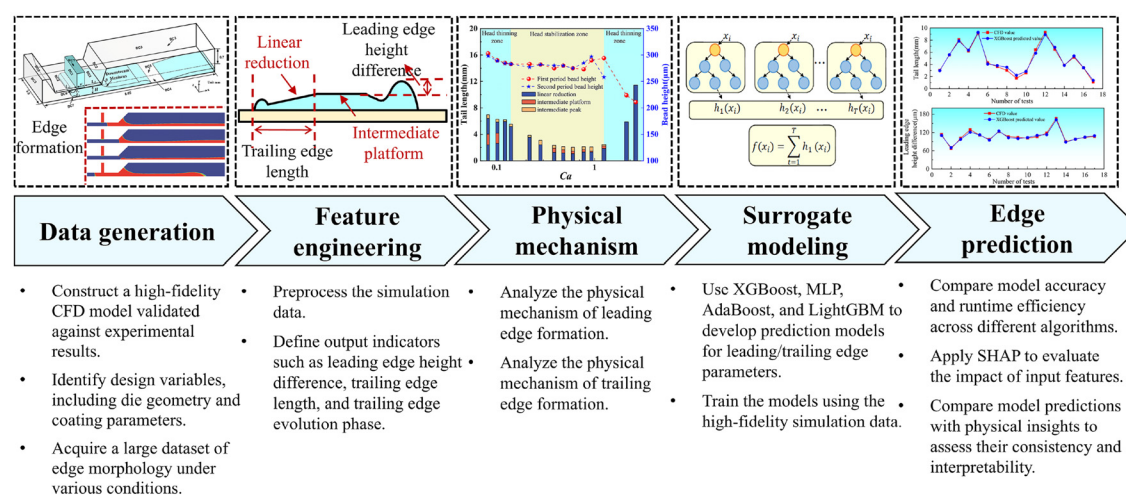


FIG. 4. Workflow for machine learning prediction of leading and trailing-edge defects.

$$\Omega(f) = \gamma T + \frac{1}{2} \lambda \sum_{j=1}^T w_j^2. \quad (19)$$

Here,  $T$  denotes the number of leaves in a tree and  $w_j$  represents the score of the  $j$ th leaf. By expanding the loss function using a second-order Taylor approximation and applying a greedy tree construction strategy, XGBoost efficiently identifies the optimal split points.

Light Gradient Boosting Machine (LightGBM)<sup>56</sup> represents a highly efficient gradient boosting decision tree (GBDT) implementation tailored for large-scale datasets. It employs a histogram-based method for constructing decision trees, discretizing continuous features into bins to significantly decrease computational costs associated with split searching and memory requirements, thereby facilitating scalable and accelerated learning

$$\text{Bin}(x_j) = \left\lfloor \frac{x_j - \min(x_j)}{\max(x_j) - \min(x_j)} \cdot B \right\rfloor, \quad (20)$$

where  $B$  is the number of bins.

To further enhance training efficiency, LightGBM incorporates gradient-based one-side sampling (GOSS), selectively preserving data instances with large gradient magnitudes to maintain model accuracy, and exclusive feature bundling (EFB), effectively reducing dimensionality by merging mutually exclusive sparse features. Additionally, LightGBM distinguishes itself by adopting a leaf-wise (best-first) tree growth strategy rather than the traditional level-wise approach, enabling the construction of more intricate models within the same tree depth. The optimization objective aligns with XGBoost's formulation [Eq. (18)].

The multi-layer perceptron (MLP)<sup>57</sup> is a classical form of feedforward neural network adept at capturing complex nonlinear relationships through layers of interconnected neurons utilizing nonlinear activation functions. It systematically performs forward propagation to calculate network outputs, subsequently leveraging the backpropagation algorithm to iteratively refine neuron weights and biases. This iterative refinement effectively reduces prediction errors. An MLP consists of multiple layers, where given an input vector  $x$ , the output  $\hat{y}$  computed by an  $L$ -layer MLP is expressed mathematically as

$$h^{(0)} = x, \quad h^{(l)} = \sigma(W^{(l)}h^{(l-1)} + b^{(l)}), \quad l = 1, 2, \dots, L, \quad (21)$$

$$\hat{y} = h^{(L)}. \quad (22)$$

Here,  $W^{(l)}$  and  $b^{(l)}$  represent the weight matrices and bias vectors at layer  $l$ , respectively, and  $\sigma(\cdot)$  denotes the nonlinear activation function.

Adaptive Boosting (AdaBoost)<sup>58</sup> is a sequential ensemble learning algorithm designed to enhance prediction accuracy by systematically combining numerous weak learners, often shallow decision trees. In each iterative stage, AdaBoost strategically increases the weights of misclassified samples, directing subsequent weak learners toward correcting previously made errors. This iterative and adaptive weighting process effectively reduces both bias and variance, yielding robust predictive capabilities. The final prediction  $H(x)$  generated by AdaBoost is calculated through a weighted majority voting scheme among the ensemble of weak learners

$$H(x) = \text{sign}\left(\sum_{t=1}^T \alpha_t h_t(x)\right), \quad (23)$$

where  $h_t(x)$  is the weak learner at iteration  $t$  and the weight  $\alpha_t$  is computed as

$$\alpha_t = \frac{1}{2} \ln \left( \frac{1 - \varepsilon_t}{\varepsilon_t} \right), \quad (24)$$

where  $\varepsilon_t$  denoting the weighted classification error. The sample distribution  $D_t(i)$  is updated after each iteration

$$D_{t+1}(i) = \frac{D_t(i) \exp(-\alpha_t y_i h_t(x_i))}{Z_t}. \quad (25)$$

$Z_t$  is a normalization factor ensuring  $\sum_i D_{t+1}(i) = 1$ .

To assess the accuracy of the prediction models, we employed the root mean square error ( $RMSE$ ), mean absolute percentage error ( $MAPE$ ), and coefficient of determination ( $R^2$ ). The definitions of these error metrics are as follows:

$$R^2 = 1 - \sum_{i=1}^n (\hat{y}_i - y_i)^2 / \sum_{i=1}^n (\bar{y}_i - y_i)^2, \quad (26)$$

$$RMSE = \sqrt{\frac{\sum_{i=1}^n (\hat{y}_i - y_i)^2}{n}}, \quad (27)$$

$$MAPE = \frac{100\%}{n} \sum_{i=1}^n \left| \frac{\hat{y}_i - y_i}{y_i} \right|. \quad (28)$$

The symbols  $y_i$ ,  $\hat{y}_i$ , and  $\bar{y}_i$  represent the observed values, predicted values, and the mean of the observed values, respectively. The smaller the  $RMSE$ , the closer the predicted values are to the observed values.  $R^2$  represents the proportion of response variation explained by the model; a value near 100% indicates that the model accounts for most of the variability. The  $MAPE$  value reflects the average of the absolute differences between the predicted and actual values, normalized by the actual values, and expressed as a percentage. A lower  $MAPE$  value indicates a higher prediction accuracy of the model.

### III. RESULTS AND DISCUSSION

#### A. Intermittent coating process

This section analyzes the mechanisms of trailing-edge formation under various conditions, based on the capillary number ( $Ca$ ). The capillary number ( $Ca$ ), a dimensionless constant that characterizes the ratio of viscous force to capillary force acting on the coating bead, is a crucial parameter in both trailing-edge formation and bead-shaping processes

$$Ca = k \frac{U_{sub}^n}{\sigma \cdot H^{n-1}}. \quad (29)$$

Figure 5 presents six cases summarizing the rupture and reformation processes of the coating bead at the trailing edge, categorized according to the capillary number ( $Ca$ ). As shown in Fig. 5(a), the formation process of the trailing edge at  $\beta = 90^\circ$  involves four stages. In the linear decrease stage (S1), as the feeding rate decreases to zero, the upstream bending liquid meniscus gradually elongates, while the downstream bending liquid meniscus is fixed to the downstream lip angle, leading to a linear decrease in coating thickness. When the upstream meniscus fractures, the coating thickness experiences a brief linear increase (S2), followed by a dynamic equilibrium stage (S3). Upon rupture of the upstream meniscus, the viscous and capillary forces within the coating bead region must reestablish equilibrium. Since the viscous

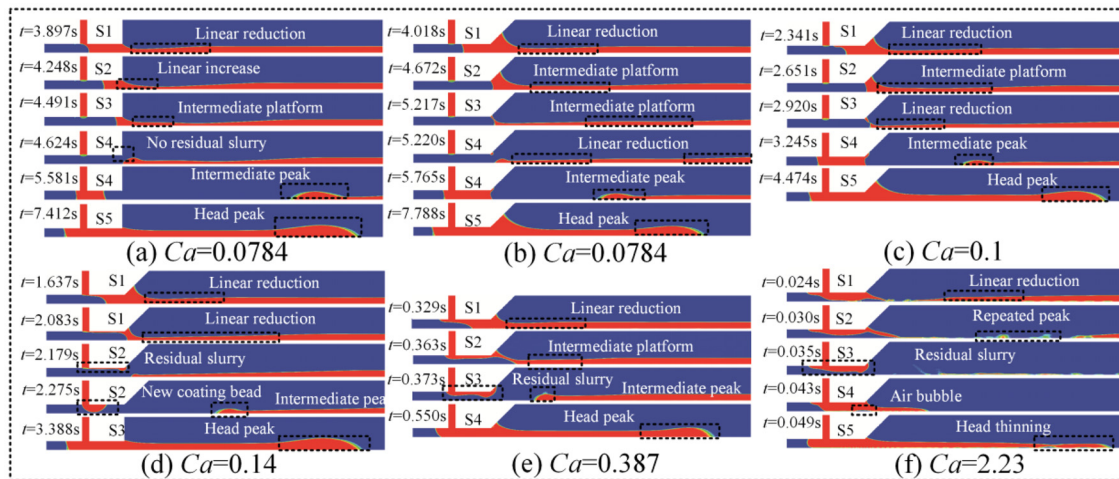


FIG. 5. Evolution of coating beads during the intermittent slot-die coating process: (a)  $\beta = 90^\circ$ , (b)–(f)  $\beta = 45^\circ$ .

force is insufficient to quickly overcome the capillary force induced by the surface tension, the movement of the upstream meniscus is hindered, causing a brief linear increase in coating thickness. When the surface tension and viscous force achieve balance, a long, intermediate plateau with constant coating thickness is formed. Subsequently, during the rupture stage (S4), the upstream and downstream bending menisci merge, and the coating bead forms an elongated liquid thread between the die and the substrate. Finally, upon rupture, the large amount of liquid present at the trailing edge contracts under the action of surface tension, with the thickness reaching an intermediate peak value (S4), and then gradually decreasing to zero, completing the tailing. As the feeding rate increases during the response time, the coating bead reforms within the gap, and the leading edge of the coating forms a head peak under the action of surface tension (S5). A similar rupture process for coating Newtonian fluids was also reported in the literature,<sup>21</sup> where the role of upstream meniscus stretching fracture in the evolution of the trailing edge is further emphasized.

As shown in Fig. 5(b), at  $\beta = 45^\circ$ , the downstream meniscus moves outside the lip and accumulates a large amount of slurry. Before the fracture of the upstream meniscus, the linear decrease stage (S1) takes place. During the fracture of the upstream meniscus, as it moves downstream and reaches the lip edge, the coating bead is in the dynamic equilibrium stage (S2), forming a longer intermediate plateau. When the upstream meniscus moves to the downstream lip edge, its wetting line is fixed by the edge constraint, while the downstream meniscus recedes toward the downstream lip angle. The coating liquid in the liquid bridge outside the lip, due to the action of surface tension, viscous force, and gravity, causes the coating thickness to undergo the S1–S2–S1 stages again and ends the tailing.

As shown in Figs. 5(c) and 5(d), a significant difference in the tailing process is observed when  $Ca$  changes from 0.1 to 0.14. First, when  $Ca = 0.1$ , the upstream meniscus fractures and moves downstream, and the tailing process only exhibits one S1–S2–S1 stage. This is because the viscous force becomes stronger as  $Ca$  increases, accelerating the fracture of the coating bead, which reduces the length of the linear decrease stage and the intermediate plateau, thus shortening the

tail length. As shown in Fig. 5(d), when  $Ca = 0.14$ , the coating thickness only experiences the linear decrease stage (S1) and the fracture shrinkage stage (S2). The upstream meniscus does not fracture prior to merging with the downstream meniscus but continues to elongate. At this point, the viscous force is sufficient to overcome the hindrance of surface tension, bypassing the dynamic equilibrium stage of coating bead evolution, and the intermediate plateau with constant coating thickness does not form. During the coating bead reorganization stage (S2), the new slurry flowing out from the gap blends with the residual slurry, forming a new coating bead.

With increasing  $Ca$ , the static contact line becomes more difficult to displace.<sup>34</sup> However, the dynamic contact line moves faster and leads to faster rupture of the coating bead. As shown in Fig. 5(e), when  $Ca = 0.387$ , during the linear decrease stage (S1), the coating thickness decreases linearly as the meniscus moves downstream. In the dynamic equilibrium stage (S2), due to the reduced influence of surface tension, the coating bead region forms an intermediate plateau with constant coating thickness under the action of the viscous force. Furthermore, with the increase in viscous force, the residual slurry in the gap between the slits increases.

As shown in Fig. 5(f), when  $Ca = 2.23$ , the residual slurry repeatedly contacts the substrate surface. The elevated viscous force destabilizes the liquid bridge at the die exit, and the resulting high shear stress causes the coating liquid to undergo repeated rupture and reconnection, forming successive peaks (S2). During the coating bead reorganization stage (S4), the new slurry flowing out from the slit exit will seal the air with the residual slurry, forming an air pocket (S4). Similar air entrainment evolution processes have been extensively reported in the prior studies.<sup>35</sup> Because the feeding rate does not reach its target value within the response time, the flow field in the coating gap downstream remains underdeveloped, resulting in thinning at the coating head.

## B. Effect of flow structure on leading and trailing edges

Figure 6 illustrates the effect of the flow structure in the coating gap on trailing-edge length and leading-edge height. First, the

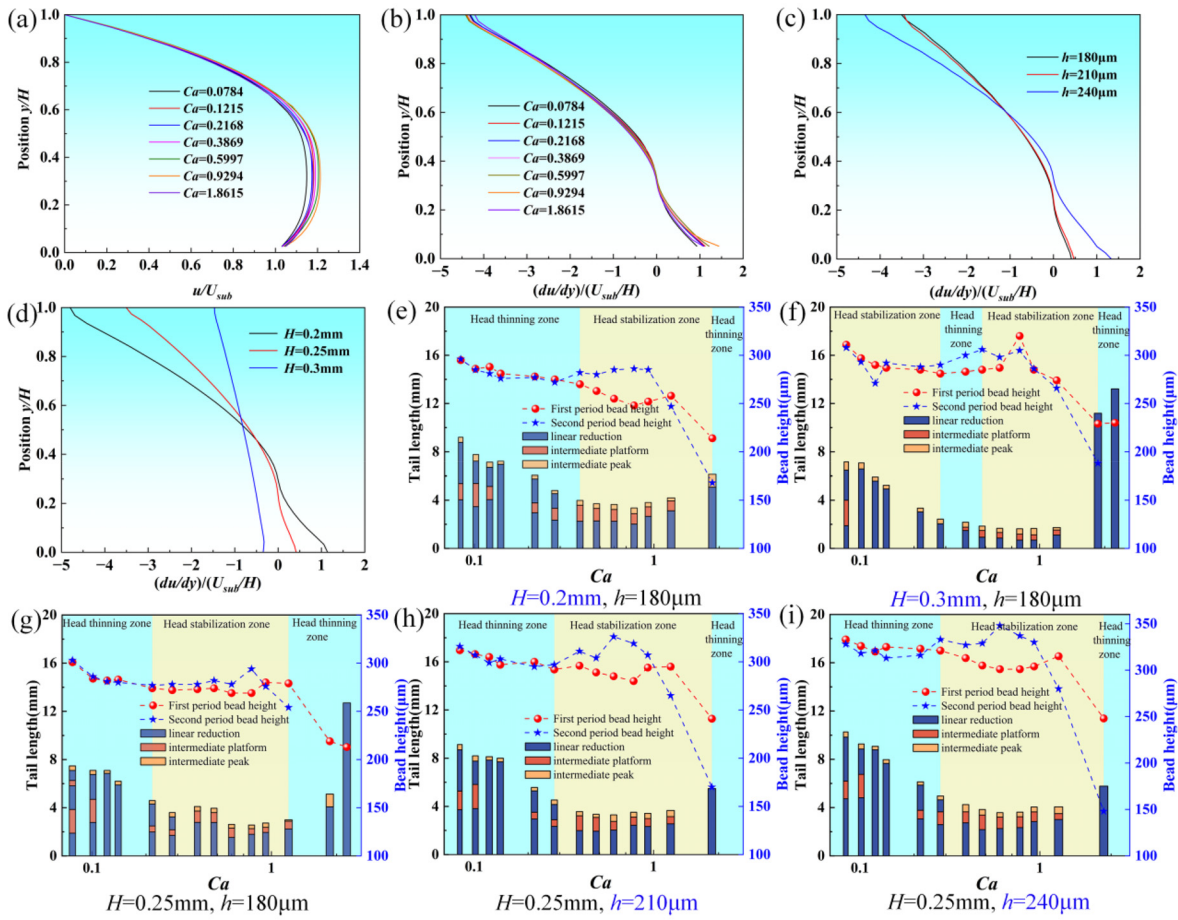


**FIG. 6.** Effect of flow structure on trailing-edge length and leading-edge height, (a)–(d) flow structures under different variables, (e)–(g) cases with the coating gap ranging from  $H = 0.2\text{--}0.3$ , (g)–(i) cases with the coating thickness ranging from  $h = 180\text{--}240$ .

relationship between the capillary number ( $Ca$ ) and the flow structure must be established. For shear-thinning fluids, the boundary layer is typically thin, and the boundary layer effect results in a pronounced velocity gradient near the upper fixed wall. As shown in Figs. 6(a)–6(d), when coating a fixed thickness film, the flow structure in the coating gap remains largely unchanged [Figs. 6(a) and 6(b)]. Therefore, the distribution of trailing-edge length and leading-edge height can be analyzed across varying  $Ca$  values under fixed coating thickness. As shown in Figs. 6(c) and 6(d), minor variations in coating thickness exert minimal influence on the flow structure. However, as the coating thickness increases, the velocity gradient increases. Increasing the coating gap reduces the velocity gradient.

As shown in the stacked bar charts in Fig. 6(e), the trailing-edge length can be roughly categorized into three regions based on  $Ca$ , with different colors indicating distinct transition phases. In the linear decrease region ( $Ca < 0.35$ ), the trailing length gradually shortens as  $Ca$  increases. At this stage, the dominant force is the capillary force induced by surface tension. As the slurry flows downstream under the action of viscous forces, the upstream meniscus moves toward the

substrate, but the capillary force resists the downstream movement of the meniscus. The strength of the capillary force depends on the dynamic contact angle.<sup>38</sup> With increasing coating speed, the capillary force decreases, leading to a gradual reduction in trailing-edge length. In the constant trailing-edge length region ( $0.35 < Ca < 0.9$ ), surface tension and viscous forces are of comparable magnitude, maintaining a constant trailing-edge length. In addition, the rear edge structure changes from “decreasing-plateau-decreasing” to “decreasing-plateau,” marking the transition in this region. At higher  $Ca$  values ( $Ca > 0.9$ ), the trailing-edge length starts to increase once more. At this point, the influence of capillary forces diminishes as the viscous force becomes the dominant force driving slurry flow. Previous studies<sup>59,60</sup> have demonstrated that, as the capillary number ( $Ca$ ) increases, the upstream meniscus undergoes significant elongation in the coating direction under low-flow-limit conditions. Likewise, when the slurry supply is halted, a higher  $Ca$  leads to an extended drainage period as the upstream meniscus detaches from the die lip. Consequently, the stretching phase of the trailing edge [Fig. 5(f)] is prolonged, and the characteristic constant-thickness plateau is no longer observed. As a

result, the overall trailing-edge length increases. Additionally, the volume of residual slurry in the coating gap increases as  $Ca$  increases. The residual slurry repeatedly contacts the substrate surface under the influence of gravity, forming a longer trailing-edge length. The trailing-edge length in this region typically exhibits irregular changes. The distribution of trailing-edge length is consistent with previously reported results for Newtonian fluids.<sup>21</sup>

As shown in Figs. 6(e)–6(g), the trailing-edge length decreases as the coating gap increases under medium and low  $Ca$  conditions. Under low  $Ca$  conditions, the smaller coating gap enhances the hindrance of capillary forces on the upstream meniscus, thus extending the trailing-edge length. Under medium  $Ca$  conditions, the smaller coating gap leads to higher pressure in the coating bead, resulting in a wider coating bead region. Therefore, the constant thickness region under smaller coating gaps is longer, leading to an increase in trailing-edge length. Under high  $Ca$  conditions, the residual slurry volume in a smaller coating gap is smaller, resulting in a shorter trailing-edge length.

As shown in Figs. 6(g)–6(i), under medium and low  $Ca$  conditions, increasing coating thickness significantly increases trailing-edge length. First, the increase in coating thickness prolongs the gradual thinning of the coating layer during trailing-edge formation, as shown in Fig. 5. Second, a higher feeding rate enlarges the coating bead volume, further contributing to the increase in trailing-edge length. However, under high  $Ca$  conditions, increasing coating thickness removes most of the slurry in the coating gap, leading to a smaller residual slurry volume and a shorter trailing-edge length.

For the first cycle leading-edge height (excluding the effects of feeding response time and residual slurry), as shown by the red line in Fig. 6(g), the  $Ca$  number divides it into four regions. In the linear decrease region ( $Ca < 0.2$ ), the leading-edge height decreases with increasing  $Ca$ . Under low  $Ca$  conditions, the increase in viscous forces increases the initial curvature of the downstream meniscus as it flows downstream, leading to a lower initial leading-edge height. Upon entering the constant height region ( $0.2 < Ca < 0.7$ ), the leading-edge height no longer changes with  $Ca$ . In the constant height region, the downstream meniscus is constrained at the lip edge as it flows downstream. As the feed rate increases and inertial forces begin to dominate, the downstream meniscus forms first.<sup>25</sup> Consequently, as  $Ca$  increases to around 1, the downstream meniscus is no longer constrained by the wetting line and extrudes directly downstream, causing a sudden increase in leading-edge height, forming a peak. During high  $Ca$  conditions, the leading-edge height decreases again. This is because the flow structure in the coating gap has not fully developed within the response time.

The red dotted line in Figs. 6(e)–6(g) shows the distribution of first-cycle leading-edge height as the coating gap changes. Under low  $Ca$  conditions ( $Ca < 0.3$ ), although reducing the coating gap increases the velocity gradient, surface tension also strengthens, so the distribution pattern of leading-edge height is unaffected. When  $0.3 < Ca < 1$ , reducing the coating gap causes the constant height region of the leading edge to transform into a decreasing region. This is because the increased velocity gradient due to the reduced coating gap increases the initial curvature of the downstream meniscus, leading to a lower initial leading-edge height. As shown in Figs. 6(e)–6(g), as  $Ca$  increases to around 1, the downstream meniscus is no longer restricted by the lip shoulder angle, and the leading-edge height becomes dependent on the coating gap. The larger the coating gap, the higher the peak value.

As shown in Figs. 6(g)–6(i), the first-cycle leading-edge height increases with film thickness.

As indicated by the blue lines in Figs. 6(e)–6(i), residual slurry significantly influences the leading-edge height during the second cycle. Under low  $Ca$  conditions ( $Ca < 0.3$ ), as illustrated in Figs. 5(a)–5(c), minimal residual slurry remains outside the lip, resulting in negligible impact on the leading-edge height. When  $Ca$  exceeds 0.3, the leading-edge height rises with further increases in  $Ca$ . As mentioned earlier, the volume of residual slurry increases with the increase in  $Ca$ . As shown by the black dashed box in S3 of Fig. 5(f), a narrow channel is formed between the residual slurry and the substrate. As shown in S4 of Fig. 5(f), during the response time of the second cycle, new slurry quickly flows downstream through the restricted channel. The residual slurry is pushed downstream by the combined effects of pressure and viscous forces. Greater amounts of residual slurry delay the development of the flow structure within the coating gap. This results in a reduced velocity gradient along the upper wall of the coating gap and may even lead to the formation of plug flow, thereby increasing the leading-edge height.

As shown in Figs. 6(e)–6(g), both increasing and decreasing the coating gap enhance the effect of residual slurry on the leading-edge height. As shown in Fig. 6(e), reducing the coating gap intensifies this effect more noticeably. This is because under a smaller coating gap, the restricted channel is narrower, and the new incoming slurry flows downstream more quickly, and the plug flow formed near the top is more readily extruded downstream. As  $Ca$  increases, the increased residual slurry exacerbating the influence of residual slurry on the leading-edge height. In contrast, under a larger coating gap, the plug flow at the upper part of the coating gap develops slowly under the action of viscous forces, which also enhances the effect of residual slurry. As shown by the blue lines in Figs. 6(g)–6(i), increasing coating thickness also promotes the increase in leading-edge height due to residual slurry. A higher inlet flow rate accelerates the expulsion of residual slurry, thereby shortening its development period. Additionally, the range of  $Ca$  values over which residual slurry exerts influence broadens. However, under high  $Ca$  conditions ( $Ca > 1$ ), the presence of residual slurry leads to a decrease in leading-edge height compared to the case where there is no residual slurry in the coating gap. At high  $Ca$  values ( $Ca > 1$ ), however, residual slurry leads to a reduction in the leading-edge height. During the initial response phase, its presence allows the coating gap to fill more rapidly, accelerating the downstream movement of the meniscus. This results in a relatively shorter formation process of the slurry flow structure, thereby increasing the velocity gradient during the feeding response time. Therefore, residual slurry causes a reduction in the second cycle leading-edge height.

The leading-edge thinning region, highlighted in yellow in Figs. 6(e)–6(i), decreases in size with a smaller velocity gradient and greater coating thickness.

Figure 7 further illustrates how leading- and trailing-edge distributions vary with geometric parameters and response times. As shown in Figs. 7(a)–7(c), a shorter die lip reduces the trailing-edge length at  $Ca < 1.2$ . This is due to a reduced slurry volume and a shorter constant-thickness platform. When  $Ca > 1.2$ , the trailing-edge length does not decrease. The residual slurry retracts into a bead-like structure under the combined effects of gravity and surface tension.<sup>61</sup> At this point, material supply continues during the response period, and the

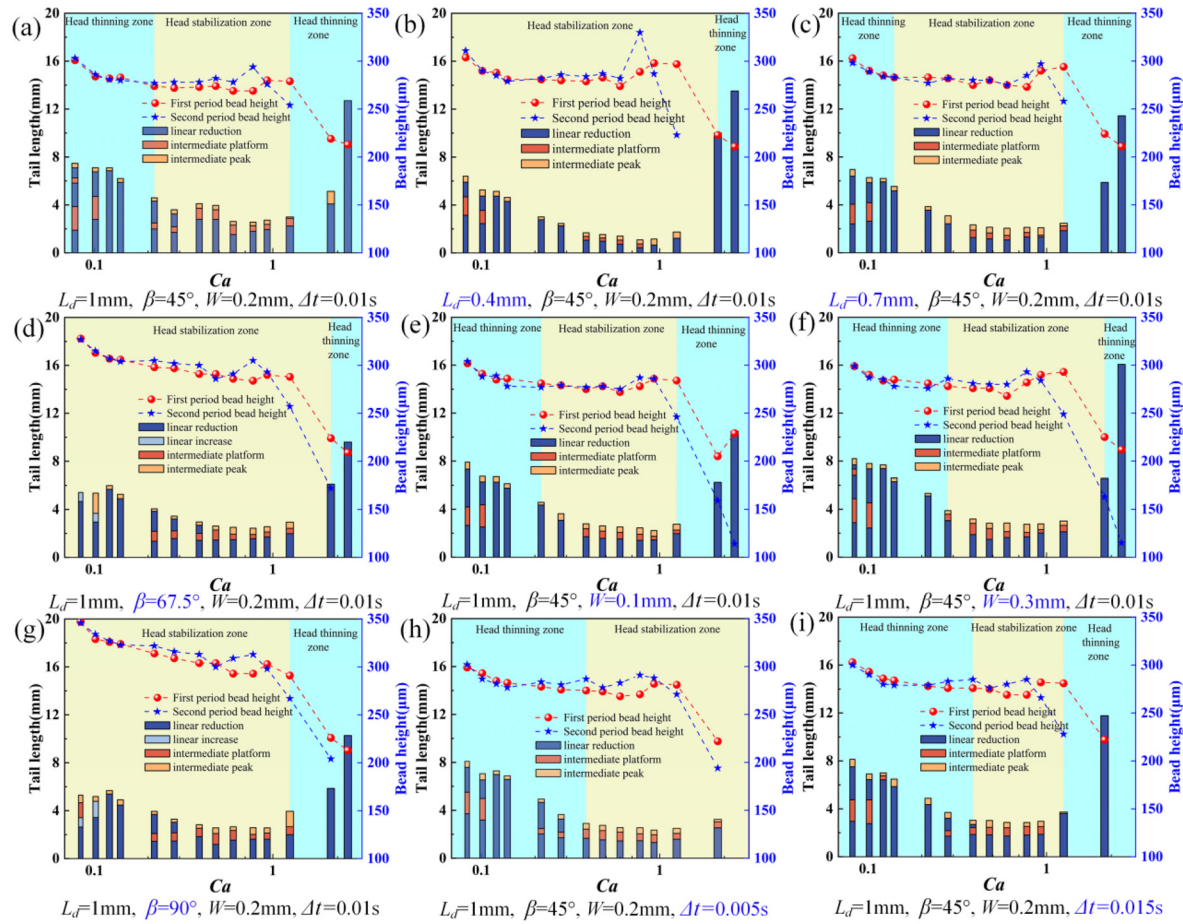


**FIG. 7.** Effects of geometry and response time on trailing-edge length and leading-edge height, (a)–(c) cases with the downstream die length ranging from  $L_d = 0.4\text{--}1$ ; (a), (d), (g) cases with the complement of the die shoulder angle ranging from  $\beta = 45^\circ$  to  $90^\circ$ ; (a), (e), (f) cases with the slot width ranging from  $W = 0.1\text{--}0.3$ ; (a), (h), (i) cases with the start-stop time ranging from  $\Delta t = 0.005\text{--}0.015$ .

bead volume increases. A shorter die lip promotes residual slurry contraction, making contact with the substrate easier and increasing the trailing-edge length. When  $Ca \approx 0.9\text{--}1.2$ , a shorter die lip enhances the leading-edge peak. This phenomenon is also observed in the leading edge of the second cycle. However, a shorter die lip is more effective in achieving a larger stable leading-edge region (yellow-filled area).

Figures 7(a), 7(d), and 7(g) show the leading and trailing-edge conditions for different die lip shoulder angles. The die lip shoulder angle is expressed as  $180^\circ - \beta$ . Under mid-low  $Ca$  conditions ( $Ca < 1$ ), a smaller die lip shoulder angle shortens the trailing edge, particularly at low  $Ca$ , by reducing both the external slurry volume and the downstream meniscus height, thereby shortening the rupture time of the meniscus liquid bridge.<sup>24</sup> When the die lip shoulder angle decreases to  $90^\circ$ , the trailing-edge length plateaus. This is attributed to the fact that the restriction of the downstream meniscus wetting line does not change with further decreases in the angle. However, decreasing the shoulder angle causes an increase in the leading-edge height. As the

shoulder angle decreases, the decrease in the wetting line height lowers the initial curvature of the downstream meniscus, which leads to an increase in the leading edge height. This also results in a larger stable leading-edge area. When the die lip shoulder angle approaches  $90^\circ$ , With no residual slurry present outside the die lip, the leading-edge height is entirely governed by internal flow dynamics, thereby enlarging the thinning region (blue-filled area).

Figures 7(a), 7(e), and 7(f) demonstrate the effects of varying slot inlet widths on the leading and trailing edges. Increasing the slot width slightly increases the trailing-edge length but has no significant effect on the leading-edge height. A wider inlet increases the size of the stable leading-edge region. Figures 7(a), 7(h), and 7(i) show the leading and trailing edges for different response times. Under high  $Ca$  conditions, reducing the response time suppresses repeated contact between residual slurry and the substrate, thereby reducing the trailing edge. However, this also results in a higher leading-edge height. This is due to the accelerated development of the velocity gradient in the coating gap as the response time shortens. A suitably extended response time

can relatively increase the velocity gradient, thereby leading to a more uniform and well-formed leading edge.

### C. Pattern evolution of the leading and trailing edges

The simulation results in Fig. 8 reveal pronounced edge effects induced by meniscus rupture during the trailing phase, whereas the

experimental observations in Fig. 9 highlight pattern formation in regions away from the edge. This discrepancy primarily arises from differences in response time during the start-stop transition. As illustrated in the rupture process (S3) in Fig. 5(b), the liquid bridge progressively thins as the upstream and downstream menisci converge while the substrate continues to move and the fluid supply is halted. In the thinning region, strong van der Waals forces can trigger film

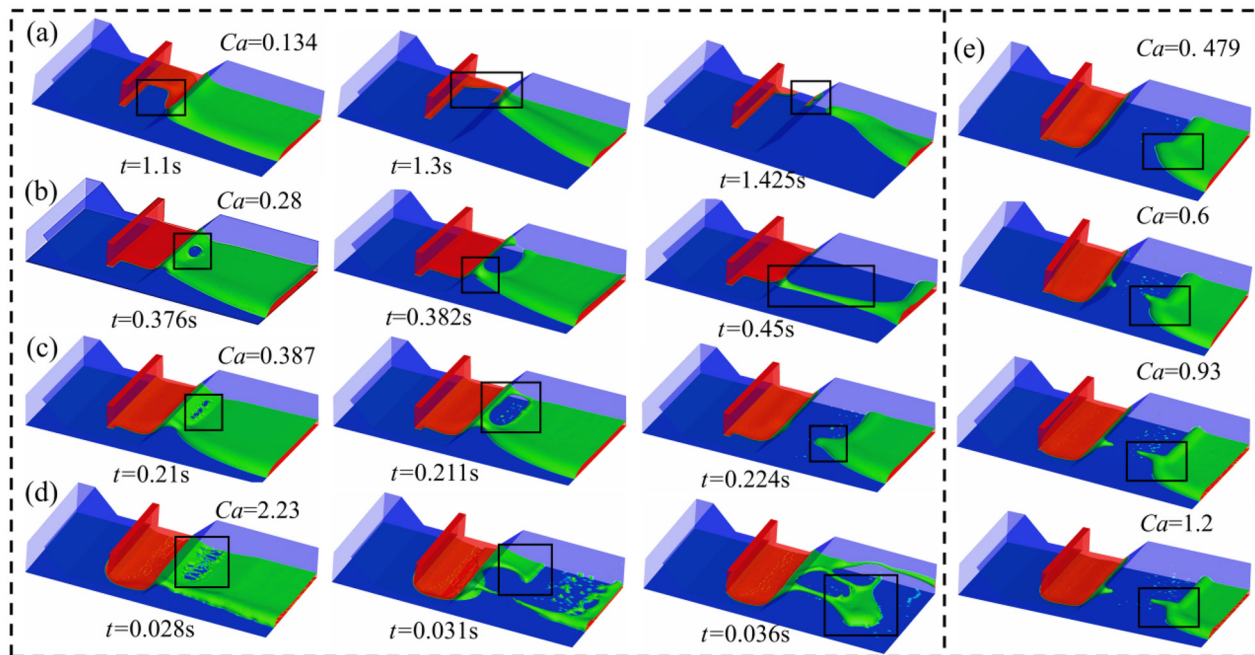


FIG. 8. Edge effects of trailing edge at different  $Ca$  (coating gap = 0.25 mm, coating thickness = 180  $\mu\text{m}$ ).

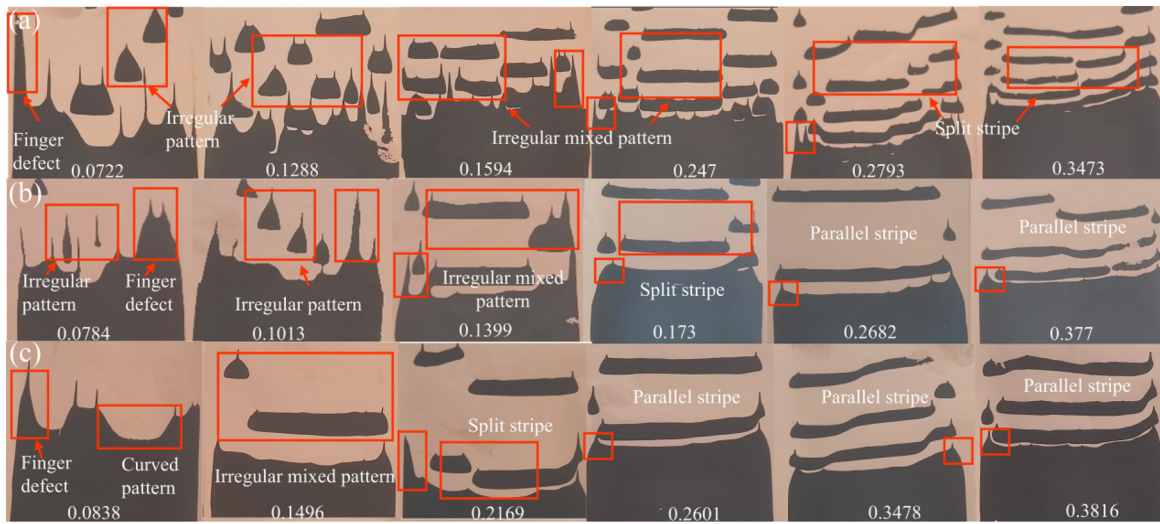


FIG. 9. Pattern evolution of trailing edge at different  $Ca$  for (a) coating gap = 0.2 mm, (b) coating gap = 0.25 mm, and (c) coating gap = 0.3 mm.

rupture.<sup>62–65</sup> Specifically, when van der Waals pressure exceeds the stabilizing force of surface tension, the locally thinned film region contracts further due to capillary suction, initiating a self-reinforcing feedback loop that results in rapid dewetting and rupture within milliseconds.

As the capillary number ( $Ca$ ) increases, the rupture location shifts further downstream, away from the die lip, thereby reducing the trailing-edge length. Figure 8 categorizes four distinct rupture modes of the coating liquid bridge. Under low  $Ca$  conditions ( $Ca < 0.387$ ), both the numerical and experimental results [Figs. 8(a), 8(b), and 9(b)] are in good agreement. In Fig. 8(a), the low coating speed causes lateral contraction of the slurry, with the downstream meniscus also retracting laterally. Due to boundary constraints, the upstream and downstream menisci coalesce near the domain edge, generating coarse fingerlike trailing structures. Figure 8(b) depicts a central rupture mode in which the liquid bridge rapidly thins under extensional stress, and rupture is induced by dominant van der Waals forces. This results in the formation of near-circular holes. Following hole formation, the residual film retracts laterally due to surface tension and extensional forces, depositing slender fingerlike defects and arc-shaped trailing edges. This rupture process often initiates simultaneously at multiple locations,<sup>63</sup> producing macroscopically irregular patterns composed of arcs and fingerlike structures. These features are consistent with the experimental observations in Fig. 9(b), where both coarse and slender fingers appear at the film edge within the range  $0.0784 < Ca < 0.1399$ .

In the intermediate regime ( $0.387 < Ca < 1.2$ ), as illustrated in Figs. 8(c) and 8(e), rupture remains governed by van der Waals forces. However, the increasing viscous resistance enhances longitudinal stretching and suppresses lateral perturbations, transforming the initially circular holes into elongated ellipses. As a result, the lateral fingerlike structures become shorter, and those in the central region vanish, consistent with experimental trends. Under high  $Ca$  conditions, shown in Fig. 8(d), the liquid bridge is instantaneously stretched to an ultrathin state by strong shear forces and subsequently breaks into multiple satellite liquid droplets.

We then examine how variations in coating gap and capillary number affect the trailing-edge morphology, as shown in Fig. 9. Based on our observations, four characteristic trailing-edge patterns are identified, described as follows:

1. Irregular patterns, corresponding to a set of randomly distributed points with tail structures in the direction of the mold movement;
2. Irregular mixed patterns, corresponding to a combination of rectangular protrusions arranged laterally and points with tail structures;
3. Split stripes, corresponding to a group of stripes that split laterally;
4. Parallel or inclined stripes perpendicular to the coating direction.

As shown by the experimental results in Fig. 9(a), under low  $Ca$  conditions, the trailing-edge pattern typically exhibits irregular dots and a gradually narrowing structure. This behavior arises because surface tension dominates over viscous forces and tends to minimize the liquid's surface area. During the trailing process, nonuniform flow at the die exit causes the coating liquid to aggregate into multiple isolated spherical droplets or protrusions under surface tension. These are subsequently stretched into irregular shapes during deposition.

As  $Ca$  increases, enhanced viscous forces lead to the formation of a more ordered pattern, consisting of laterally aligned rectangular blocks and isolated dots along the coating direction. Compared to the disordered structures at low  $Ca$ , the block-like trailing edge at medium  $Ca$  appears significantly more regular. Strong viscous resistance inhibits the free redistribution of the liquid, particularly in slower-flow regions where the liquid accumulates into droplets. In faster-flow regions, the liquid is stretched more thinly, forming well-defined block structures.

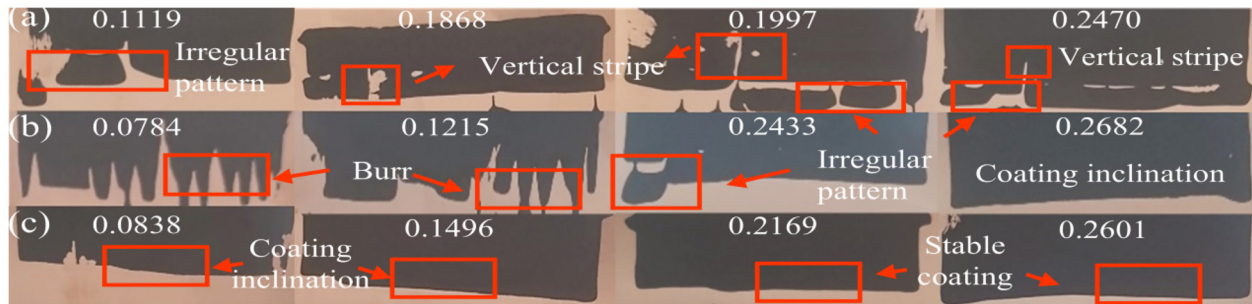
With further increases in coating speed, pronounced viscous effects suppress flow instabilities, causing the rectangular protrusions to transition into slender, split-like stripes with a slight horizontal tilt. Previous studies have shown that under low-flow-rate conditions, stripe spacing increases with coating speed.<sup>32</sup> However, during trailing-edge formation, an opposite trend is observed: the stripe spacing decreases as coating speed rises, accompanied by an increase in stripe number and a reduction in stripe width, consistent with earlier reports.<sup>61</sup> We infer that the observed stripe inclination is not due to variations in coating gap height but rather results from spontaneously occurring defects in the line pattern—likely related to shear slip phenomena.<sup>30</sup>

As shown in Figs. 9(b) and 9(c), increasing the coating gap gradually reduces and eventually eliminates irregular pattern features. On the one hand, a larger gap limits the ability of spherical droplets to contact the substrate. On the other hand, it reduces the velocity gradient within the coating gap, allowing the fluid to maintain higher viscosity under low shear, which counteracts surface tension and promotes smoother flow. As the gap increases, split-like stripes evolve into more regular, parallel bands. In contrast, a smaller gap amplifies the internal velocity gradient, generating greater shear stress and making lateral splitting of the liquid more likely. With continued gap expansion, stripe width and spacing increase, stripe count decreases, and the patterns gradually transition into evenly spaced, parallel stripes.

Figure 10 illustrates the leading-edge morphology under different coating gaps. At a 0.2 mm gap [Fig. 10(a)], the leading edge exhibits irregular liquid droplets, accompanied by foil leakage and vertical voids. As  $Ca$  increases, the overall defect morphology remains largely unchanged. The narrow gap restricts the evolution and coalescence of spherical residual slurry; consequently, multiple isolated droplets contact the substrate before merging, producing irregular deposits and vertical streaks in the coating.

When the gap is increased to 0.25 mm [Fig. 10(b)], the leading-edge morphology shifts to a jagged, inclined shape. Although the larger gap facilitates residual slurry coalescence, surface tension drives the slurry to form a wavy interface. Upon contact with the substrate, this surface translates into a serrated leading edge. This observation aligns with earlier reports attributing cone-shaped leading edges to residual slurry accumulation.<sup>35</sup> As  $Ca$  increases, enhanced viscous forces begin to suppress the self-organizing behavior driven by surface tension, gradually smoothing the leading edge.

At a 0.3 mm coating gap [Fig. 10(c)], split-like features at the coating edge disappear entirely, though a noticeable inclination remains. This is attributed to asymmetric lateral growth of the coating bead, which causes the leading edge to contact the substrate at an angle. As  $Ca$  increases, the prolonged merging time combined with higher viscous forces further smooths the coating bead surface, gradually eliminating the inclined features.

FIG. 10. Pattern evolution of leading edge at different  $Ca$ : (a) coating gap = 0.2 mm, (b) coating gap = 0.25 mm, and (c) coating gap = 0.3 mm.TABLE II. Details of the parameters of the evaluation criteria. Boldface denotes the best value, i.e., highest  $R^2$  or lowest MAPE/RMSE.

| Models  | $R^2$         |       |          |          | MAPE         |        |              |          | RMSE         |      |          |          |
|---------|---------------|-------|----------|----------|--------------|--------|--------------|----------|--------------|------|----------|----------|
|         | XGBoost       | MLP   | AdaBoost | LightGBM | XGBoost      | MLP    | AdaBoost     | LightGBM | XGBoost      | MLP  | AdaBoost | LightGBM |
| Model-1 | <b>98.3%</b>  | 97.8% | 96.9%    | 96.5%    | <b>7.58%</b> | 9.1%   | 8.68%        | 10.68%   | <b>0.31</b>  | 0.35 | 0.42     | 0.44     |
| Model-2 | <b>95.8%</b>  | 87.5% | 90.7%    | 83%      | <b>4.64%</b> | 13.68% | 14.3%        | 16.27%   | <b>6.83</b>  | 18.1 | 15.6     | 21.1     |
| Model-3 | <b>91.35%</b> | 11.1% | 89%      | 72.5%    | 5.58%        | 21.39% | <b>4.21%</b> | 13.32%   | <b>0.125</b> | 0.35 | 0.136    | 0.219    |

#### D. Leading- and trailing-edge defect feature prediction

In this section, we developed three predictive models: trailing-edge length (Model-1), leading-edge height difference (Model-2), and trailing-edge evolution phase (Model-3), using XGBoost, MLP, AdaBoost, and LightGBM algorithms, respectively. The surrogate models incorporate a total of seven input variables and three output targets. The input set includes four operational parameters and three geometric parameters of the coating die, all selected to reduce the response time during the start-stop process. Table I lists the seven input variables along with their respective levels. For predicting the trailing-edge evolution phase, we employed a composite approach involving two surrogate models to estimate the occurrence frequency of each phase. For example, if the decreasing phase appears twice and the platform phase once, the evolution phase is classified as decreasing-platform-decreasing.

Each of the four algorithms was used to build prediction models based on a dataset comprising 728 total samples. Each surrogate model was trained on 182 samples. In light of the limited data size, a strict fourfold cross-validation (fourfold CV) strategy was adopted to prevent overfitting in the machine learning models. The original dataset was pre-split into 80% for training, 10% for validation, and 10% for independent testing. Initially, a combination of grid search and four-fold CV was applied to the training set to systematically optimize model hyperparameters; the optimal configurations are reported in Appendix D, as shown in Table IV. Subsequently, the training and validation sets were merged into a combined 90% dataset, and an additional fourfold CV was performed to further enhance model robustness. The RMSE loss curves for both training and validation sets during cross-validation are presented in Appendix D, as shown in Fig. 15. The results indicate that the models converged well, exhibiting

minimal discrepancies between training and validation losses, and no divergence was observed. This outcome confirms that none of the machine learning models suffered from overfitting during training. To gain insight into the influence of each input variable, we employed Shapley values—a local interpretability method that quantifies the contribution of each feature to individual predictions. Shapley values from the test set were analyzed to evaluate the global impact of each variable across all samples. The complete dataset used in this study has been made publicly available.

The model performance comparison for predicting trailing-edge length (Model-1), leading-edge height difference (Model-2), and trailing-edge evolution stage (Model-3) is summarized in Tables II and III. Among the evaluated models, XGBoost consistently demonstrated superior performance across all three prediction tasks, particularly in estimating trailing-edge length and evolution stage, where it achieved the highest accuracy and lowest error. However, a significantly greater computational burden was observed when predicting leading-edge height difference. The MLP and LightGBM models achieved acceptable accuracy for trailing-edge length but exhibited substantial

TABLE III. Details of the running time.

| Models  | Running time (s) |       |          |          |
|---------|------------------|-------|----------|----------|
|         | XGBoost          | MLP   | AdaBoost | LightGBM |
| Model-1 | 9.37             | 4.76  | 3.97     | 4.78     |
| Model-2 | 97.9             | 332.5 | 4.55     | 4.55     |
| Model-3 | 99.37            | 14.2  | 61       | 373.33   |

performance degradation in the other two tasks, with increased errors and reduced stability. Although the AdaBoost model showed relatively consistent performance, its prediction errors remained comparatively high. Considering both accuracy and computational efficiency, XGBoost is identified as the most suitable model for this study.

Figures 11(a)–11(d) illustrate the global SHAP summary plots generated using the XGBoost model, including beeswarm diagrams and corresponding bar charts of feature importance. Figures 11(e) and 11(f) present the model's prediction results. In these visualizations, the horizontal axis represents SHAP values, reflecting the marginal contribution of each feature to the model output, while the vertical axis lists the input features. Each dot denotes a data instance, color-coded according to feature value (blue: low, red: high). The right-hand bar

charts display the mean absolute SHAP values [Mean(|SHAP|)], providing a quantitative assessment of feature importance.

As shown in Fig. 11(a), coating speed exerts the most significant influence on the prediction of leading-edge height difference in the second coating cycle, evidenced by its wide SHAP distribution and high average contribution. Interaction effects are also apparent. For example, high-coating speed may cause the downstream meniscus to extrude from the die lip, markedly increasing the leading-edge height. This effect is further modulated by the capillary number ( $Ca$ ), coating gap ( $H$ ), and die shoulder angle ( $180^\circ - \beta$ ). While a smaller shoulder angle can reduce the leading-edge height, its overall impact is limited.

Figure 11(b) reveals that the capillary number and coating speed are the primary determinants of trailing-edge length, playing a

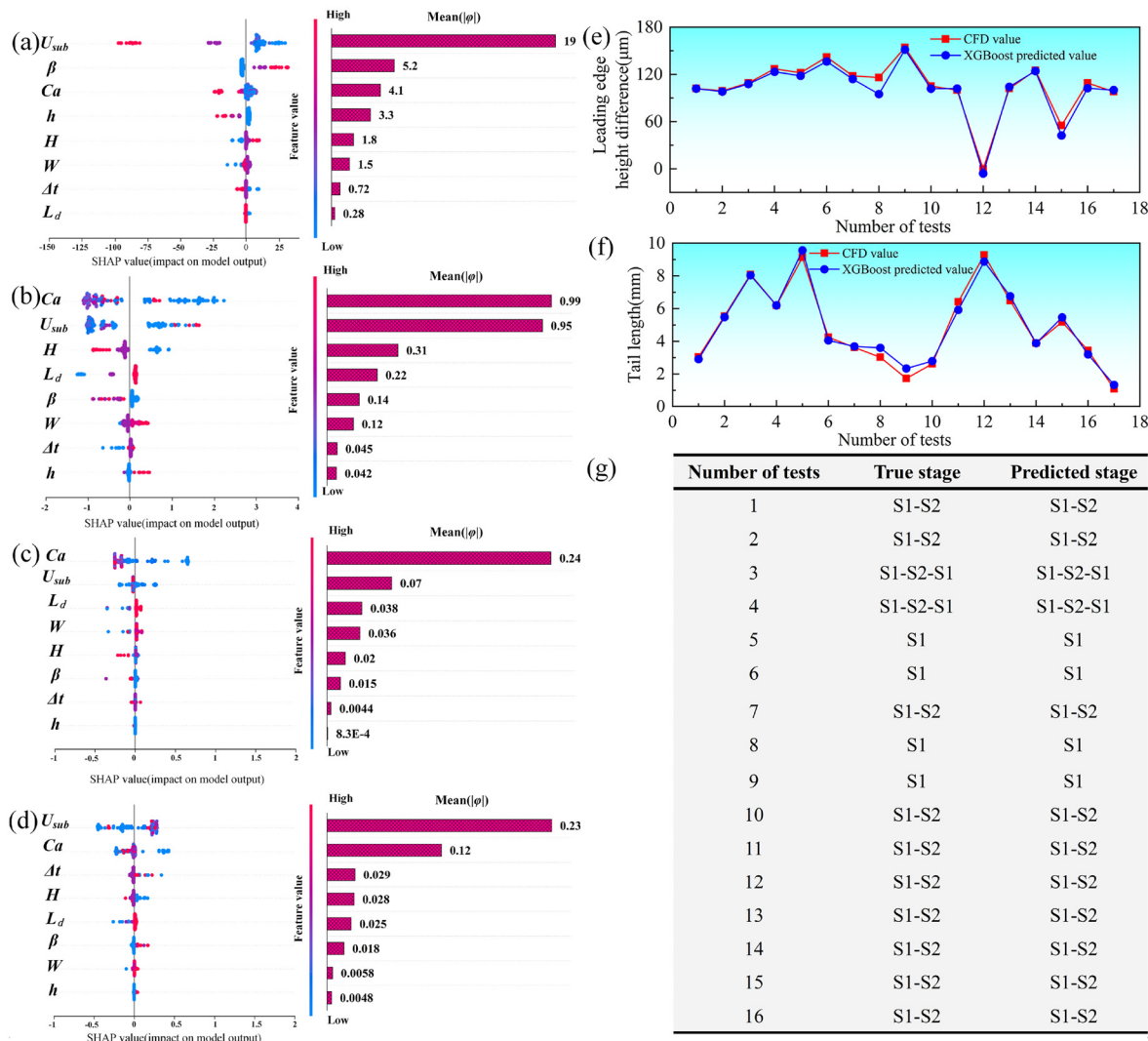


FIG. 11. Shapley values for the seven input variable samples predicted using the XGBoost algorithm: (a) leading-edge height difference, (b) trailing-edge length, (c) reduction phase, and (d) plateau phase. The heatmap illustrates the intensity of the Shapley values for the samples, while the bar charts display the average absolute Shapley values, representing the importance of the input variables. (e)–(g) Compare the predicted results with the CFD results.

dominant role in regulating the drainage dynamics of the coating bead. Among geometric parameters, coating gap ( $H$ ) exhibits a clear negative correlation with trailing-edge length, while downstream die lip length shows a positive association—consistent with previous physical analyses. Figures 11(c) and 11(d), corresponding to the shrinkage and plateau phases of the trailing edge, respectively, confirm the persistent dominance of  $Ca$  and coating speed, whereas the contributions of other variables are minimal.

In summary, the SHAP-based analysis provides clear insights into the relative importance of input features in determining coating-edge defect dimensions. Overall, the capillary number and coating speed emerge as the most influential predictors, surpassing geometric factors in predictive significance. Notably, for the second-cycle leading-edge height difference, the die shoulder angle proves more critical than  $Ca$ , underscoring its role in regulating leading-edge formation. For both trailing-edge length and its evolution stage,  $Ca$  and coating speed consistently dominate. These findings align well with the underlying physical mechanisms and offer practical guidance for optimizing key process parameters to ensure coating uniformity and product performance consistency in industrial applications.

#### IV. SUMMARY

This study is the first to integrate high-fidelity multiphase flow simulations with machine learning techniques to systematically investigate the transient formation mechanisms of leading- and trailing-edge defects during intermittent slot-die coating for lithium-ion battery electrodes. The analysis highlights the critical role of meniscus dynamics in defect formation. Furthermore, quantitative relationships between coating parameters and defect dimensions were established, and high-accuracy predictive models were developed. The major conclusions are as follows:

- (1) The relationship between trailing-edge length and capillary number ( $Ca$ ) can be categorized into three distinct regimes, each corresponding to different trailing-edge evolution stages. Both  $Ca$  and coating speed strongly influence the stretching and rupture of the upstream meniscus. During the stretching phase, the trailing-edge length decreases approximately linearly, stabilizing at a plateau upon rupture. Enhanced viscous forces accelerate meniscus breakup, maintaining a nearly constant trailing-edge length. Geometric-induced reductions in coating bead volume also shorten the trailing edge. Specifically, under low-to-moderate  $Ca$  conditions, decreasing the die lip length from 1.0 to 0.4 mm and increasing the coating gap from 0.2 to 0.3 mm resulted in trailing-edge length reductions of approximately 35%–140% and 22%–58%, respectively. Under high  $Ca$  conditions ( $Ca > 1$ ), shortening the response time during the start-stop phase becomes necessary.
- (2) The leading-edge height exhibits four characteristic regimes as a function of  $Ca$ , largely determined by the velocity gradient within the coating gap and the volume of residual slurry. Increased viscous forces reduce the leading-edge height until equilibrium is reached with surface tension, after which the height stabilizes. When the downstream meniscus is not constrained by a wetting line, the leading-edge height becomes directly correlated with the coating gap—larger gaps result in significantly higher peak heights. Under viscosity-dominated conditions, increasing residual slurry volume raises the leading-

edge height; however, under high  $Ca$  conditions, additional slurry can reduce the height. Expanding the stable leading-edge region can be achieved by limiting the downstream wetting line or decreasing bead volume. In particular, reducing both the die lip length and the die shoulder angle increased the stable region area by approximately 89%, although the latter also caused an increase in height variation of 17%–46%.

- (3) Fingerlike edges, arc-shaped, and stripe patterns observed on the trailing edge are directly linked to four distinct meniscus liquid-bridge rupture mechanisms. The length of fingering defects first decreases and then stabilizes as viscous forces increase—an observation consistent with experimental findings. As  $Ca$  increases, the 3D morphology of the trailing-edge transitions from irregular droplets to alternating rectangular structures and ultimately to transverse streaks. Elevated viscosity effectively suppresses streak splitting. Additionally, higher coating speeds or smaller coating gaps promote increased streak density and lateral instability. Burrs and tilting defects observed at the leading edge during the second coating cycle are attributed to residual slurry evolution during re-initiation, which can be mitigated by increasing either the coating gap or slurry viscosity.
- (4) Four machine learning models—XGBoost, MLP, AdaBoost, and LightGBM—were developed based on high-fidelity CFD simulation data. A fourfold cross-validation strategy was employed to prevent overfitting. Among them, XGBoost demonstrated the best predictive performance for leading-edge height difference, trailing-edge length, and trailing-edge evolution stage. The respective  $R^2$ , MAPE, and RMSE values were 0.958, 0.0464, and 6.83 for leading-edge height difference; 0.983, 0.0758, and 0.31 for trailing-edge length; and 0.9135, 0.0558, and 0.125 for trailing-edge stage classification. SHAP-based interpretability analysis further confirmed that  $Ca$  and coating speed are the dominant control parameters, in strong agreement with theoretical understanding.

Although this study represents the first application of machine learning to predict edge defect dimensions in intermittent slot-die coating, the ultimate goal is the full digitalization of the coating process. Future research should focus on quantitatively characterizing meniscus dynamics and constructing a comprehensive feature library to establish robust mappings between process features and defect types or coating uniformity. Integrating these insights with advanced machine learning frameworks offers a promising pathway toward the development of a digital twin for slot-die coating.

#### ACKNOWLEDGMENTS

The work was supported by grants from the Research Project Supported by Shanxi Scholarship Council of China (Grant No. 2021-137), the Fundamental Research Program of Shanxi Province (Grant No. 202103021224273), and the Postgraduate Education Innovation Project in Shanxi Province of China (Grant No. 2023KY640).

#### AUTHOR DECLARATIONS

##### Conflict of Interest

The authors have no conflicts to disclose.

**Author Contributions**

**Xiaosong Gong:** Conceptualization (equal); Formal analysis (equal); Methodology (equal); Software (equal); Writing – original draft (equal). **Bin Li:** Software (equal); Visualization (equal). **Jiaye Yao:** Software (equal); Visualization (equal). **Fei Yan:** Data curation (equal); Investigation (equal); Writing – review & editing (equal). **Xiaozhong Du:** Funding acquisition (equal); Supervision (equal).

**DATA AVAILABILITY**

The data that support the findings of this study are openly available in figshare at [10.6084/m9.figshare.28407527](https://doi.org/10.6084/m9.figshare.28407527), Ref. 66.

**APPENDIX A: COMPUTATIONAL MESH**

As depicted in Fig. 12, a nonuniform cell distribution is employed in the x-y plane, resulting in the generation of approximately 4 000 000 cells. A second-order explicit scheme is used to resolve the transient terms, while pressure and gradients are

discretized using the PRESTO and Least Squares cell-based methods. The Geo-Reconstruct method is applied to establish a comprehensive interface. To resolve the discretized pressure–velocity coupling equations, we utilize the SIMPLEC method. An adaptive time-stepping approach is implemented to keep the global Courant number below 0.5, thereby ensuring the accuracy of the simulation.

**APPENDIX B: MODEL VALIDATION**

To validate the numerical model, we compared the normalized coating thickness and pressure during the trailing-edge formation process, as illustrated in Fig. 13, with previously published experimental results.<sup>9</sup> The parameters for the fluid included a density of  $1320 \text{ kg/m}^3$ , surface tension of  $0.066 \text{ N/m}$ , static contact angle of  $26^\circ$ , and equilibrium contact angle of  $36^\circ$ .<sup>21</sup> The fluid viscosity was characterized using a non-Newtonian power-law model, with the index  $k$  and power-law index  $n$  set to 1.13 and 0.56, respectively. The experimental slit width  $W$  was 0.5 mm. Figure 13(a) presents a comparison of the normalized coating thickness of the trailing edge

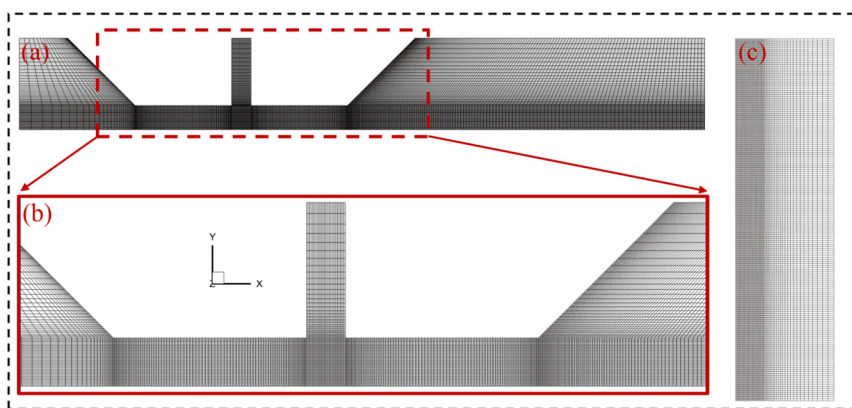


**FIG. 12.** Mesh cell distribution: (a) front view; (b) zoomed-in local view; and (c) left view.

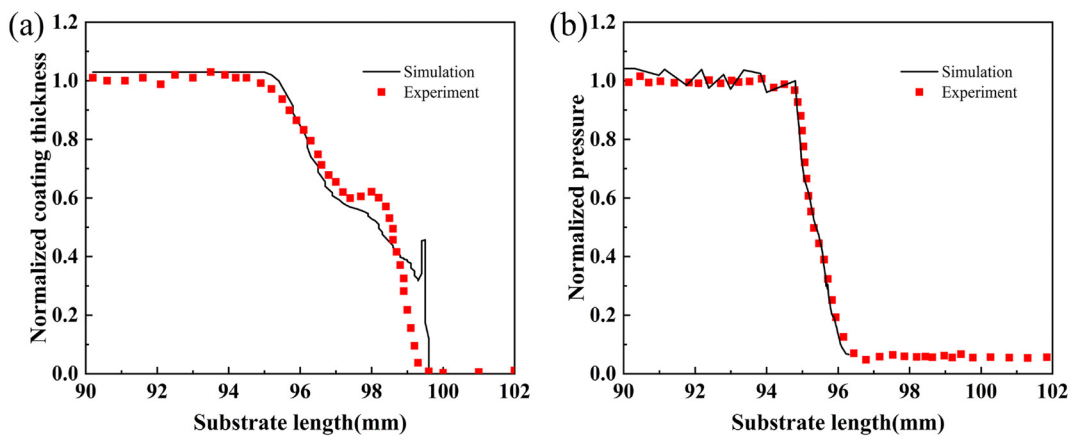


**FIG. 13.** Comparisons of the numerical and experimental results at coating speed = 20 m/min and ideal coating thickness =  $153.6 \mu\text{m}$ : (a) the normalized coating thickness of trailing edges and (b) the normalized pressure in the slot during the forming process of trailing edges.

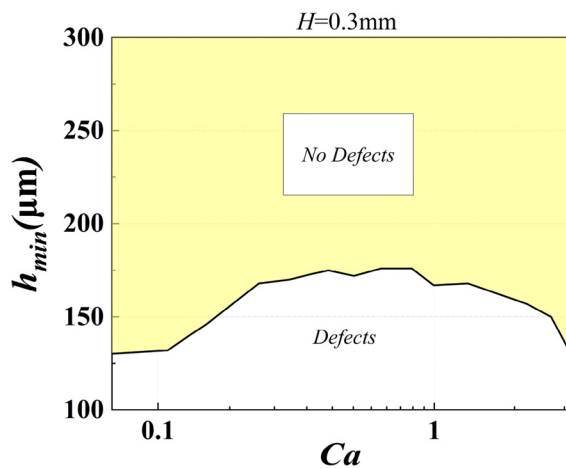


FIG. 14. The minimum coatable wet film thickness ( $H = 0.3$  mm).

from both numerical results and experimental data at a coating speed of  $V_{sub} = 20$  m/min and an ideal coating thickness of  $h = 153.6 \mu\text{m}$ . Both the numerical and experimental coating thicknesses initially decrease linearly, then reach a plateau, followed by a subsequent decrease. The experimental results are slightly higher

than the numerical solutions in the range of 97–98 mm. This discrepancy primarily arises from differences in the downstream lip geometry and the measurement locations. In the simulation, the lip edge is modeled as straight, while manufacturing errors in the experiment lead to unavoidable rounding. As discussed in Sec. III A, the rounded corner on the downstream lip elevates the wetted line position of the downstream meniscus, resulting in an increased height of the coating thickness plateau. Additionally, due to the limitations of the computational domain, the simulated results reflect the immediate extraction of the trailing edge following the breakup of the coating bead, whereas measurements in the experiment occur after a longer time interval. Under the influence of surface tension, the trailing edge further contracts, and the descent length diminishes.

#### APPENDIX C: COATING WINDOW

Figure 14 shows the minimum coatable wet film thickness ( $H = 0.3$  mm).

#### APPENDIX D: LOSS CURVES AND HYPERPARAMETER

Figure 15 shows the RMSE loss curves for both training and validation sets during cross-validation. Table IV lists final hyperparameter combinations for ML models.

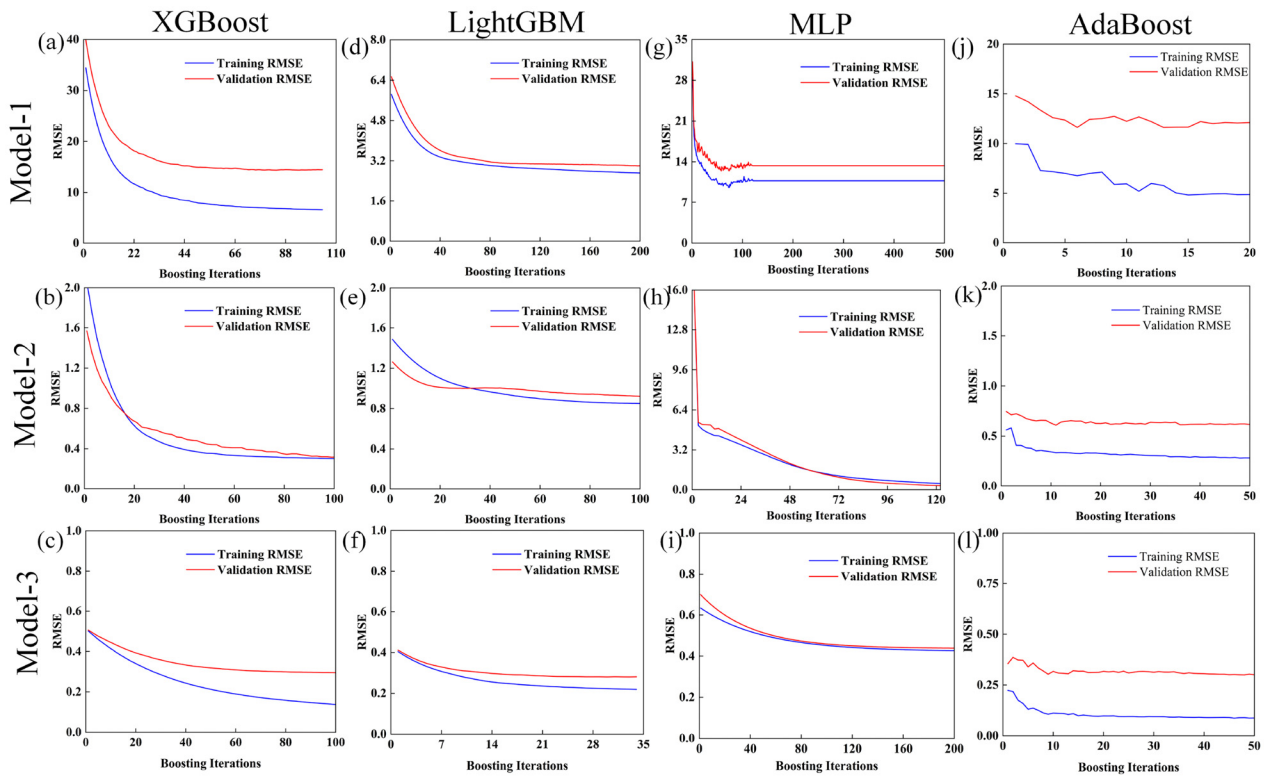


FIG. 15. The RMSE loss curves for both training and validation sets during cross-validation.

**TABLE IV.** Final hyperparameter combinations for ML models.

|                    | Models  |       |          |          |         |      |          |          |         |      |          |          |
|--------------------|---------|-------|----------|----------|---------|------|----------|----------|---------|------|----------|----------|
|                    | Model-1 |       |          |          | Model-2 |      |          |          | Model-3 |      |          |          |
|                    | XGBoost | MLP   | AdaBoost | LightGBM | XGBoost | MLP  | AdaBoost | LightGBM | XGBoost | MLP  | AdaBoost | LightGBM |
| n_estimator        | 100     | ...   | 50       | 100      | 200     | ...  | 20       | 200      | 100     | ...  | 150      | 150      |
| max_depth          | 3       | ...   | 7        | 7        | 3       | ...  | 7        | 5        | 7       | ...  | 5        | 5        |
| learning_rate      | 0.1     | ...   | 0.01     | 0.05     | 0.1     | ...  | 0.01     | 0.05     | 0.05    | ...  | 0.1      | 0.1      |
| colsample_bytree   | 0.8     | ...   | ...      | 1        | 0.8     | ...  | ...      | ...      | 0.9     | ...  | ...      | 0.9      |
| subsample          | 0.8     | ...   | ...      | 1        | 1       | ...  | ...      | ...      | 0.9     | ...  | ...      | 0.8      |
| activation         | ...     | relu  | ...      | ...      | ...     | tanh | ...      | ...      | ...     | relu | ...      | ...      |
| alpha              | ...     | 0.001 | ...      | ...      | ...     | 0.1  | ...      | ...      | ...     | 0.01 | ...      | ...      |
| hidden_layer_sizes | ...     | 100   | ...      | ...      | ...     | 100  | ...      | ...      | ...     | 50   | ...      | ...      |
| learning_rate_init | ...     | 0.01  | ...      | ...      | ...     | 0.01 | ...      | ...      | ...     | 0.1  | ...      | ...      |

## REFERENCES

- <sup>1</sup>J. H. Kim, N. Y. Kim, Z. Ju, Y. K. Hong, K. D. Kang, J. H. Pang, S. J. Lee, S. S. Chae, M. S. Park, J. Y. Kim, G. Yu, and S. Y. Lee, "Upscaling high-areal-capacity battery electrodes," *Nat. Energy* **10**, 295–307 (2025).
- <sup>2</sup>K. Liu, B. Ouyang, X. Guo, Y. Guo, and Y. Liu, "Advances in flexible organic field-effect transistors and their applications for flexible electronics," *npj Flexible Electron.* **6**, 1–19 (2022).
- <sup>3</sup>S. M. Raupp, L. Merklein, M. Pathak, P. Scharfer, and W. Schabel, "An experimental study on the reproducibility of different multilayer OLED materials processed by slot die coating," *Chem. Eng. Sci.* **160**, 113–120 (2017).
- <sup>4</sup>S. Yuan, D. Zheng, T. Zhang, Y. Wang, F. Qian, L. Wang, X. Li, H. Zheng, Z. Diao, P. Zhang, T. Pauporté, and S. Li, "Scalable preparation of perovskite films with homogeneous structure via immobilizing strategy for high-performance solar modules," *Nat. Commun.* **16**, 2052 (2025).
- <sup>5</sup>G. R. Cagnani, G. Ibáñez-Redín, B. Tirich, D. Gonçalves, D. T. Balogh, and O. N. Oliveira, Jr., "Fully-printed electrochemical sensors made with flexible screen-printed electrodes modified by roll-to-roll slot-die coating," *Biosens. Bioelectron.* **165**, 112428 (2020).
- <sup>6</sup>T. J. Jeong, X. Yu, and T. A. L. Harris, "Scaled production of functionally graded thin films using slot die coating on a roll-to-roll system," *ACS Appl. Mater. Interfaces* **16**, 9264–9274 (2024).
- <sup>7</sup>J. Kurfer, M. Westermeier, C. Tammer, and G. Reinhart, "Production of large-area lithium-ion cells—Preconditioning, cell stacking and quality assurance," *CIRP Ann. Manuf. Technol.* **61**, 1–4 (2012).
- <sup>8</sup>G. Reinhart and J. Kurfer, *Handhaben in Der Batteriefertigung-Forschungs-Und Demonstrationszentrum Für Lithium-Ionen-Zellen* (Springer-VDI-Verlag, 2011), pp. 545–550.
- <sup>9</sup>R. Diehm, H. Weinmann, J. Kumberg, M. Schmitt, J. Fleischer, P. Scharfer, and W. Schabel, "Edge formation in high-speed intermittent slot-die coating of disruptively stacked thick battery electrodes," *Energy Technol.* **8**, 1900137 (2019).
- <sup>10</sup>K. J. Ruschak, "Limiting flow in a pre-metered coating device," *Chem. Eng. Sci.* **31**, 1057–1060 (1976).
- <sup>11</sup>B. G. Higgins and L. E. Scriven, "Capillary pressure and viscous pressure drop set bounds on coating bead operability," *Chem. Eng. Sci.* **35**, 673–682 (1980).
- <sup>12</sup>S. H. Lee, H. J. Koh, B. K. Ryu, S. J. Kim, H. W. Jung, and J. C. Hyun, "Operability coating windows and frequency response in slot coating flows from a viscoelastic model," *Chem. Eng. Sci.* **66**, 4953–4959 (2011).
- <sup>13</sup>I. Jang and S. Song, "A model for prediction of minimum coating thickness in high-speed slot coating," *Int. J. Heat Fluid Flow* **40**, 180–185 (2013).
- <sup>14</sup>F. O. Silva, I. R. Siqueira, M. S. Carvalho, and R. L. Thompson, "Slot coating flows with a Boussinesq-Scriven viscous interface," *Phys. Fluids* **35**, 042106 (2023).
- <sup>15</sup>I. R. Siqueira, R. L. Thompson, M. S. Carvalho, and P. R. de Souza Mendes, "Slot coating of viscoplastic materials: A computational study of the effects of viscoplasticity on the flow dynamics and low-flow limit," *J. Non-Newtonian Fluid Mech.* **327**, 105222 (2024).
- <sup>16</sup>Z. Fang, Y. Yan, C. Li, X. Luo, and P. Zhou, "Bubble defect generation mechanism in slot die coating of high-viscosity fluids," *ACS Appl. Mater. Interfaces* **16**, 11890–11900 (2024).
- <sup>17</sup>S. Kumar, "Liquid transfer in printing processes: Liquid bridges with moving contact lines," *Annu. Rev. Fluid Mech.* **47**, 67–94 (2015).
- <sup>18</sup>S. Dodds, M. S. Carvalho, and S. Kumar, "The dynamics of three-dimensional liquid bridges with pinned and moving contact lines," *J. Fluid Mech.* **707**, 521–540 (2012).
- <sup>19</sup>A. Moghadam and H. V. Tafreshi, "On liquid bridge adhesion to fibrous surfaces under normal and shear forces," *Colloids Surf. A* **589**, 124473 (2020).
- <sup>20</sup>L. Wang and T. J. McCarthy, "Shear distortion and failure of capillary bridges. Wetting information beyond contact angle analysis," *Langmuir* **29**, 7776–7781 (2013).
- <sup>21</sup>P. Tan, S. Diao, T. Huang, Z. Yang, H. Zhou, and Y. Zhang, "Mechanism and control of the trailing edge in intermittent slot die coating," *Ind. Eng. Chem. Res.* **59**, 15758–15767 (2020).
- <sup>22</sup>D. Maza and M. S. Carvalho, "Trailing edge formation during slot coating of rectangular patches," *J. Coat. Technol. Res.* **14**, 1003–1013 (2017).
- <sup>23</sup>M. Schmitt, R. Diehm, P. Scharfer, and W. Schabel, "An experimental and analytical study on intermittent slot die coating of viscoelastic battery slurries," *J. Coat. Technol. Res.* **12**, 927–938 (2015).
- <sup>24</sup>Y. R. Chang, C. F. Lin, and T. J. Liu, "Start-up of slot die coating," *Polym. Eng. Sci.* **49**, 1158–1167 (2009).
- <sup>25</sup>S. Pan, Y. Wei, J. Chen, C. Wu, and J. Jia, "Simulation analysis of the start-up process of Carreau-type fluid slot die coating," *J. Coat. Technol. Res.* **21**, 1281–1289 (2024).
- <sup>26</sup>J. S. Park, S. Jee, B. Chun, and H. W. Jung, "Practical operations for intermittent dual-layer slot coating processes," *Korea-Aust. Rheol. J.* **34**, 181–186 (2022).
- <sup>27</sup>M. Schmitt, *Slot Die Coating of Lithium-Ion Battery Electrodes* (KIT Scientific Publishing, 2016).
- <sup>28</sup>M. Kasischke, S. Hartmann, K. Niermann, M. Smarra, D. Kostyrin, U. Thiele, and E. L. Gurevich, "Pattern formation in slot-die coating," *Phys. Fluids* **35**, 074117 (2023).
- <sup>29</sup>W. Tewes, M. Wilczek, S. V. Gurevich, and U. Thiele, "Self-organized dip-coating patterns of simple, partially wetting, nonvolatile liquids," *Phys. Rev. Fluids* **4**, 123903 (2019).
- <sup>30</sup>V. S. Mitlin, "Dewetting of solid surface: Analogy with spinodal decomposition," *J. Colloid Interface Sci.* **156**, 491–497 (1993).
- <sup>31</sup>U. Thiele, M. G. Velarde, and K. Neuffer, "Dewetting: Film rupture by nucleation in the spinodal regime," *Phys. Rev. Lett.* **87**, 016104 (2001).
- <sup>32</sup>M. A. Y. H. Lam, L. J. Cummings, and L. Kondic, "Stability of thin fluid films characterised by a complex form of effective disjoining pressure," *J. Fluid Mech.* **841**, 925–951 (2018).

- <sup>33</sup>S. M. Raupp, M. Schmitt, A. L. Walz, R. Diehm, H. Hummel, P. Scharfer, and W. Schabel, "Slot die stripe coating of low viscous fluids," *J. Coat. Technol. Res.* **15**, 899–911 (2018).
- <sup>34</sup>A. W. Parsekian and T. A. Harris, "Extrusion on-demand pattern coating using a hybrid manufacturing process," *Chem. Eng. Process. Process Intensif.* **109**, 20–31 (2016).
- <sup>35</sup>K. L. Bhamidipati, S. Didari, P. Bedell, and T. A. L. Harris, "Wetting phenomena during processing of high-viscosity shear-thinning fluid," *J. Non-Newtonian Fluid Mech.* **166**, 723–733 (2011).
- <sup>36</sup>S. Khandavalli and J. P. Rothstein, "The effect of shear-thickening on the stability of slot-die coating," *AIChE J.* **62**, 4536–4547 (2016).
- <sup>37</sup>M. Schmitt, M. Baunach, L. Wengeler, K. Peters, P. Junges, P. Scharfer, and W. Schabel, "Slot-die processing of lithium-ion battery electrodes—Coating window characterization," *Chem. Eng. Process. Process Intensif.* **68**, 32–37 (2013).
- <sup>38</sup>T. Huang, P. Tan, Z. Zhong, M. Li, Y. Zhang, and H. Zhou, "Numerical and experimental investigation on the defect formation in lithium-ion-battery electrode-slot coating," *Chem. Eng. Sci.* **258**, 117744 (2022).
- <sup>39</sup>E. Ayerbe, M. Berecibar, S. Clark, A. A. Franco, and J. Ruhland, "Digitalization of battery manufacturing: Current status, challenges, and opportunities," *Adv. Energy Mater.* **12**, 2102696 (2022).
- <sup>40</sup>X. Yue, J. Chen, Y. Li, X. Li, H. Zhu, and Z. Yin, "Intelligent control system for droplet volume in inkjet printing based on stochastic state transition soft actor-critic DRL algorithm," *J. Manuf. Syst.* **68**, 455–464 (2023).
- <sup>41</sup>H. Zhang and S. K. Moon, "Reviews on machine learning approaches for process optimization in noncontact direct ink writing," *ACS Appl. Mater. Interfaces* **13**, 53323–53345 (2021).
- <sup>42</sup>T. Lombardo, M. Duquesnoy, H. El-Bouysidy, F. Arévalo, A. Gallo-Bueno, P. B. Jorgensen, A. Bhowmik, A. Demortière, E. Ayerbe, F. Alcaide, M. Reynaud, J. Carrasco, A. Grimaud, C. Zhang, T. Vegge, P. Johansson, and A. A. Franco, "Artificial intelligence applied to battery research: Hype or reality?," *Chem. Rev.* **122**, 10899–10969 (2022).
- <sup>43</sup>M. Jiang, Y. Zhang, Z. Yang, H. Li, J. Li, J. Li, T. Lu, C. Wang, G. Yang, and L. Pan, "A data-driven interpretable method to predict capacities of metal ion doped TiO<sub>2</sub> anode materials for lithium-ion batteries using machine learning classifiers," *Inorg. Chem. Front.* **10**, 6646–6654 (2023).
- <sup>44</sup>S. Hagh, M. F. V. Hidalgo, M. F. Niri, R. Daub, and J. Marco, "Machine learning in lithium-ion battery cell production: A comprehensive mapping study," *Batteries Supercaps* **6**, e202300046 (2023).
- <sup>45</sup>C. Reynolds, M. Faraji Niri, M. F. Hidalgo, R. Heymer, L. Roman, G. Alsofi, H. Khanom, B. Pye, J. Marco, and E. Kendrick, "Impact of formulation and slurry properties on lithium-ion electrode manufacturing," *Batteries Supercaps* **7**, e202300396 (2023).
- <sup>46</sup>C. Tan, R. Ardanese, E. Huemiller, W. Cai, H. Yang, J. Bracey, and G. Pozzato, "Data-driven battery electrode production process modeling enabled by machine learning," *J. Mater. Process. Technol.* **316**, 117967 (2023).
- <sup>47</sup>J. Schnell, C. Nentwich, F. Endres, A. Kollenda, F. Distel, T. Knoche, and G. Reinhart, "Data mining in lithium-ion battery cell production," *J. Power Sources* **413**, 360–366 (2019).
- <sup>48</sup>M. F. Niri, C. Reynolds, L. A. R. Ramirez, E. Kendrick, and J. Marco, "Systematic analysis of the impact of slurry coating on manufacture of Li-ion battery electrodes via explainable machine learning," *Energy Storage Mater.* **51**, 223–238 (2022).
- <sup>49</sup>S. K. Seo, H. Kim, A. Samadi, M. Atwair, J. Hong, B. Kang, H. Yim, and C. J. Lee, "Surrogate optimization of lithium-ion battery coating process," *J. Cleaner Prod.* **447**, 141064 (2024).
- <sup>50</sup>C. W. Hirt and B. D. Nichols, "Volume of fluid (VOF) method for the dynamics of free boundaries," *J. Comput. Phys.* **39**, 201–225 (1981).
- <sup>51</sup>J. U. Brackbill, D. B. Kothe, and C. Zemach, "A continuum method for modeling surface tension," *J. Comput. Phys.* **100**, 335–354 (1992).
- <sup>52</sup>A. Hoffmann, S. Spiegel, T. Heckmann, P. Scharfer, and W. Schabel, "CFD model of slot die coating for lithium-ion battery electrodes in 2D and 3D with load balanced dynamic mesh refinement enabled with a local-slip boundary condition in OpenFOAM," *J. Coat. Technol. Res.* **20**, 3–14 (2023).
- <sup>53</sup>A. Ashish Saha and S. K. Mitra, "Effect of dynamic contact angle in a volume of fluid (VOF) model for a microfluidic capillary flow," *J. Colloid Interface Sci.* **339**, 461–480 (2009).
- <sup>54</sup>B. G. Marcot and A. M. Hanea, "What is an optimal value of k in k-fold cross-validation in discrete Bayesian network analysis?," *Comput. Stat.* **36**, 2009–2031 (2021).
- <sup>55</sup>T. Chen and C. Guestrin, "XGBoost: A scalable tree boosting system," in *Proceedings of the 22nd ACM SIGKDD International Conference on Knowledge Discovery and Data Mining* (ACM, 2016), pp. 785–794.
- <sup>56</sup>G. Ke, Q. Meng, T. Finley, T. Wang, W. Chen, W. Ma, Q. Ye, and T. Y. Liu, "LightGBM: A highly efficient gradient boosting decision tree," in *Advances in Neural Information Processing Systems 30* (NIPS, 2017).
- <sup>57</sup>D. E. Rumelhart, G. E. Hinton, and R. J. Williams, "Learning representations by back-propagating errors," *Nature* **323**, 533–536 (1986).
- <sup>58</sup>Y. Freund and R. E. Schapire, "A decision-theoretic generalization of on-line learning and an application to boosting," *J. Chin. Comput. Syst.* **55**, 119–139 (1997).
- <sup>59</sup>N. V. Mhatre, M. S. Carvalho, and S. Kumar, "Delaying dynamic wetting failure using thermal Marangoni flow," *Phys. Rev. Fluids* **7**, 124002 (2022).
- <sup>60</sup>E. Vandré, M. S. Carvalho, and S. Kumar, "Delaying the onset of dynamic wetting failure through meniscus confinement," *J. Fluid Mech.* **707**, 496–520 (2012).
- <sup>61</sup>H. Kang, J. Park, and K. Shin, "Statistical analysis for the manufacturing of multi-strip patterns by roll-to-roll single slot-die systems," *Rob. Comput. Integr. Manuf.* **30**, 363–368 (2014).
- <sup>62</sup>D. Moreno-Boza, A. Martínez-Calvo, and A. Sevilla, "Stokes theory of thin-film rupture," *Phys. Rev. Fluids* **5**, 014002 (2020).
- <sup>63</sup>T. P. Witelski and A. J. Bernoff, "Dynamics of three-dimensional thin film rupture," *Physica D* **147**, 155–176 (2000).
- <sup>64</sup>N. V. Mhatre and S. Kumar, "Shear-induced depinning of thin droplets on rough substrates," *J. Fluid Mech.* **990**, A14 (2024).
- <sup>65</sup>N. V. Mhatre and S. Kumar, "Pinning–depinning transition of droplets on inclined substrates with a three-dimensional topographical defect," *Soft Matter* **20**, 3529–3540 (2024).
- <sup>66</sup>See <http://10.6084/m9.figshare.28407527> for "figshare."